

Molecular Bubble and Outflow in S Mon Revealed by Multiband Datasets

DEJIAN LIU,^{1,2} YE XU,^{1,2} YINGJIE LI,¹ ZEHAO LIN,^{1,2} CHAOJIE HAO,^{1,2} WENJIN YANG,^{3,4} JINGJING LI,^{1,2} XINRONG LIU,^{1,2}
YIWEI DONG,^{1,2} SHUAIBO BIAN,^{1,2} AND DEYUN KONG⁵

¹*Purple Mountain Observatory, Chinese Academy of Sciences, Nanjing 210023, People's Republic of China*

²*School of Astronomy and Space Science, University of Science and Technology of China, Hefei 230026, People's Republic of China*

³*School of Astronomy & Space Science, Nanjing University, 163 Xianlin Avenue, Nanjing 210023, People's Republic of China*

⁴*Max-Planck-Institut für Radioastronomie, auf dem Hügel 69, 53121 Bonn, Germany*

⁵*School of Physics, Harbin Institute of Technology, Harbin 150001, People's republic of China*

ABSTRACT

We identify a molecular bubble, and study the star formation and its feedback in the S Mon region, using multiple molecular lines, young stellar objects (YSOs), and infrared data. We revisit the distance to S Mon, $\sim 722 \pm 9$ pc, using *Gaia* Data Release 3 parallaxes of the associated Class II YSOs. The bubble may be mainly driven by a massive binary system (namely 15 Mon), the primary of which is an O7V-type star. An outflow is detected in the shell of the bubble, suggesting ongoing star formation activities in the vicinity of the bubble. The total wind energy of the massive binary star is three orders of magnitude higher than the sum of the observed turbulent energy in the molecular gas and the kinetic energy of the bubble, indicating that stellar winds help to maintain the turbulence in the S Mon region and drive the bubble. We conclude that the stellar winds of massive stars have an impact on their surrounding environment.

Keywords: Interstellar molecules (849) – Young stellar objects (1834) – Stellar wind bubbles (1635)

1. INTRODUCTION

The mass-loss phase is a very common phenomenon during the early evolutionary stages of a star. Strong winds from young stars inject momentum and energy into the surrounding environment, thus affecting the dynamics and structure of their parent clouds (e.g., Lada 1985; Arce et al. 2011; Frank et al. 2014; Bally 2016; Li et al. 2020). High-mass stars evolve very quickly and they may still be embedded in their parent cloud when they reach the main-sequence stage. When a high-mass star forms in the molecular cloud, its ultraviolet (UV) radiation can ionize and heat the surrounding gas to create an H_{II} region. The expanding H_{II} region can reshape the surrounding molecular gas and drive a bubble (e.g., Churchwell et al. 2006; Zhang et al. 2015). During the main-sequence stage, high-mass stars can drive spherical winds that blow away the gas around the star and then form bubbles (e.g., Castor et al. 1975; Arce et al. 2011). Bubbles and outflows are common stellar-feedback phenomena in the star-formation process and provide information about the physical properties of their surroundings (e.g., Lada 1985; Arce et al. 2010, 2011; Li et al. 2018, 2020).

There have been quite a few studies concerned with bubbles, outflows and their feedback (e.g., see Frank et al. 2014; Dale 2015; Bally 2016, for reviews). Since directly measuring the proper motion of extended structures, like molecular clouds, is very difficult, many previous studies only analyzed the line-of-sight dynamics in a region. Additionally, recent studies started to investigate the 3D structure of molecular clouds in the solar neighborhood (e.g., Green et al. 2019; Lallement et al. 2019; Guo et al. 2021), mainly enabled by the *Gaia* space mission (Gaia Collaboration et al. 2016). Young stellar objects (YSOs) that only recently formed in star-forming molecular clouds are still close to their birth sites; hence, they still, on average, share the distance and kinematic properties of their parent clouds (e.g., Fűrész et al. 2008; Tobin et al. 2009; Hacar et al. 2016; Großschedl et al. 2021). On this basis, cloud distances can be estimated

by using the distances of YSOs located within the clouds as proxies (e.g., [Großschedl et al. 2018, 2021](#); [Zhang 2023](#)). The recent release of astrometric data from *Gaia* Data Release 3 (DR3, [Gaia Collaboration et al. 2023](#)) allows one to obtain a large number of high-quality parallaxes and proper motions of nearby YSOs, which also makes it possible to explore further the 3D kinematics of molecular clouds that harbor these YSOs (e.g., [Großschedl et al. 2021](#); [Flaccomio et al. 2023](#)).

NGC 2264 is a nearby high-mass star-forming complex in Monoceros with a distance of about 700–800 pc (e.g., [Zucker et al. 2020](#); [Flaccomio et al. 2023](#)), and it is well studied at multiple wavelengths (for a review see [Dahm 2008](#)). Studies of the spatial and dynamical structure of NGC 2264 revealed that it is composed of two complexes: S Mon in the northern part and the Cone Nebula in the southern part (e.g., [Sung et al. 2008](#); [Tobin et al. 2015](#); [Venuti et al. 2018](#)). The gas structure of S Mon is dominated by massive stars at its center. For instance, 15 Mon, which consists of an O7V primary star with a mass of $35 M_{\odot}$ and an O9.5V secondary star with a mass of $24 M_{\odot}$ ([Dahm 2008](#)). 15 Mon exhibits variations in its UV resonance line profile as well as fluctuations in its soft X-ray flux, which can be interpreted as being induced by variations in its mass-loss rate ([Snow et al. 1981](#); [Grady et al. 1984](#); [Dahm 2008](#)).

[Sung & Bessell \(2010\)](#) and [Venuti et al. \(2018\)](#) studied the star formation history of S Mon by analyzing the properties of young clusters, and found that stars are still forming actively in the region. [Buckle et al. \(2012\)](#) found that the CO emission surrounding S Mon shows many filaments and arcs, and these structures are unlikely due to protostellar outflow activity. Based on ^{13}CO emission, [Tobin et al. \(2015\)](#) speculated that there exists a bubble in the S Mon region which may be driven by 15 Mon. Since studies of the S Mon region either used only young stars or molecular gas, or did not focus on the details of the bubble, the properties of this region, especially the bubble, outflows, and their feedback remain unclear.

In this work, we carried out molecular line observations and collected YSO information in the S Mon region, aiming to provide insights into the star formation activities and their feedback. This paper is organized as follows. In Section 2, we present the data used in this work. The correlation between YSOs and molecular gas, the distance of the molecular gas, and details of the bubble and outflow are presented in Section 3. We discuss the driving source of the bubble and the energy cascade in S Mon, as well as the kinematic features of the bubble based on the YSOs in Section 4. In Section 5, we summarize the main results.

2. DATA

2.1. *Molecular Gas*

Molecular line observations of S Mon were carried out between 2022 April and November using the Purple Mountain Observatory Delingha (PMODLH) 14 m millimeter-wavelength telescope. Four molecular lines were observed: ^{12}CO ($J = 1 - 0$), ^{13}CO ($J = 1 - 0$), C^{18}O ($J = 1 - 0$), and HCO^+ ($J = 1 - 0$). The three CO lines were observed simultaneously. All lines were observed with the nine-beam Superconducting Spectroscopic Array Receiver system in the sideband separation mode ([Shan et al. 2012](#)), with the ^{13}CO and C^{18}O lines in the lower sideband and the ^{12}CO and HCO^+ lines in the upper sideband. The on-the-fly (OTF; [Sun et al. 2018](#)) mode was used during the observations, and the OTF raw data were gridded in fits cube with a pixel size of $30''$ using the GILDAS software package ([Pety 2005](#)).¹ The typical integration time per position was approximately 3 minutes. Each fast Fourier transform spectrometer with a bandwidth of 1 GHz provides 16 384 channels, yielding a spectral resolution of 61 kHz.² All results presented in this work are expressed as brightness temperatures, $T_{\text{R}}^* = T_{\text{A}}^*/\eta_{\text{mb}}$, where T_{A}^* is the antenna temperature and η_{mb} is the main beam efficiency. Table 1 lists the observational parameters of the molecular lines.

2.2. *Young Stellar Object Sample*

The classification of YSOs was initially proposed by [Lada & Wilking \(1984\)](#) to delineate their evolutionary stages, and is defined as follows. Class I YSOs are protostars that are still embedded in an envelope and surrounded by a circumstellar disk, causing significant infrared-excess and a rising slope of the spectral energy distribution (SED) in the mid- to far-infrared range; Class II YSOs are pre-main-sequence (PMS) stars with circumstellar disks, which show a negative SED slope, that is significantly above the slopes of main-sequence stars (see [Lada et al. 2006](#)). Class II YSOs

¹ <http://www.iram.fr/IRAMFR/GILDAS>

² <http://www.radioast.nscd.cn/english/zhuangtaibaogao.php>

Table 1. Observational Parameters of the Molecular Lines

Molecular line (J = 1 - 0) (1)	Rest frequency (GHz) (2)	HPBW ($''$) (3)	T_{sys} (K) (4)	η_{mb} (5)	δ_v (km s^{-1}) (6)	rms noise (K) (7)
^{12}CO	115.271	50	250 – 300	51.1%	0.159	0.15
^{13}CO	110.201	52	150 – 200	56.3%	0.166	0.07
C^{18}O	109.782	52	150 – 200	56.3%	0.166	0.06
HCO^+	89.189	59	100 – 150	58.1%	0.187	0.03

NOTE—(1) Molecular line. (2) Frequency of the molecular line. (3) Half-power beamwidth (HPBW). (4) Typical system temperature. (5) Main beam efficiency. (6) Velocity resolution. (7) Main beam rms noise.

with inner holes in their accretion disks are named transition disks and Class III YSOs are PMS stars surrounded by thin disk remnants (anaemic disks, ADs) or they could be already disk free.

To study the young cluster NGC 2264, a variety of multiwavelength datasets and criteria have been employed to identify the evolutionary stages of YSOs. For example, [Sung et al. \(2008, 2009\)](#) classified YSOs based on SED slopes of infrared data combined with X-ray data from the *Chandra X-ray Observatory* ([Weisskopf et al. 2002](#)). [Broos et al. \(2013\)](#) adopted a Naive Bayes approach to classify YSOs, using data from the Massive Young star-forming Complex Study in Infrared and X-rays (MYStIX) project ([Feigelson et al. 2013](#)). [Cody et al. \(2014\)](#) classified YSOs based on the slope of SEDs at near- and mid-infrared wavelengths. [Rapson et al. \(2014\)](#) utilized a color-based classification scheme to classify YSOs with *Spitzer* ([Fazio et al. 2004](#)) data and Two Micron All Sky Survey (2MASS; [Skrutskie et al. 2006](#)) photometry. [Venuti et al. \(2018\)](#) classified YSOs using spectroscopic and photometric data from the *Gaia*-ESO Survey (GES, [Gilmore et al. 2012](#); [Randich et al. 2013](#)) and the Coordinated Synoptic Investigation of NGC 2264 Survey (CSI 2264, [Cody et al. 2014](#)).

We describe in detail the YSO data collection, classification criteria, and astrometric parameters acquisition in Appendix A, and briefly introduce these procedures here. We collected YSO candidates in the S Mon region from [Sung et al. \(2009\)](#), [Broos et al. \(2013\)](#), [Cody et al. \(2014\)](#) and [Rapson et al. \(2014\)](#), within an area of $202.8^\circ < l < 203.1^\circ$, and $2.0^\circ < b < 2.3^\circ$. Duplicates were eliminated through coordinate cross-matching with a radius of $1''$, yielding in an initial sample of 1023 YSO candidates. As these candidates were classified by different methods, we reclassified them through a homogeneous classification scheme based on infrared data. We adopted the SED slope ($\alpha = d \log \lambda F_\lambda / d \log \lambda$, [Lada 1987](#)) and the classification scheme of [Greene et al. \(1994\)](#) to classify the evolutionary stage of the YSOs. Flat-spectrum sources are classified as Class II YSOs in this study. In line with [Sung et al. \(2009\)](#), we use $\alpha \geq 0.3$ to classify objects as Class I and -1.8 to 0.3 for Class II. When using selection criteria based on infrared photometry, only the part of Class III YSOs with infrared-excess (i.e., ADs) can be classified. Therefore, X-ray data collected by [Flaccomio et al. \(2023\)](#) were also employed to classify additional Class III YSOs. The Class III YSOs in this work are comprised of sources with ADs and disk-less PMS stars. For the former, the lower limit for a source with infrared-excess is given by [Lada et al. \(2006\)](#) with $\alpha > -2.56$. This slope is typical for stellar photospheres when there is no additional infrared-excess from a disk present, and when using the *Spitzer* IRAC bands to calculate the infrared SED (see e.g., [Lada et al. 2006](#); [Teixeira et al. 2012](#)). Given the uncertainties in photometry, however, we took -2.3 as a rough limit to exclude possible contaminants from field stars. For disk-less PMSs, they have a SED slope of below -2.3 and X-ray emission. The SED fitting was performed without reddening corrections following [Cody et al. \(2014\)](#). In this case, we gain a sample of seven Class I, 160 Class II, and 245 Class III YSOs (101 ADs + 144 disk-less PMSs). The parallaxes and proper motions of these YSOs were taken from *Gaia* DR3 ([Gaia Collaboration et al. 2023](#)). The radial velocities (RVs) of the YSOs were collected from the Sloan Digital Sky Survey (SDSS) DR17 APOGEE-2 ([Abdurro'uf et al. 2022](#)) and the catalog of [Tobin et al. \(2015\)](#).

To summarize, we end up with a sample of one Class I, 145 Class II, and 231 Class III YSOs that had matched with the *Gaia* DR3 catalog, and 47 Class II and 91 Class III YSOs with available RV information.

To compare the gas and stellar RVs, the heliocentric RVs (V_{Helio}) of the YSOs were converted to the local standard of rest velocity (V_{LSR}). We followed the conversion method described by Reid et al. (2009) via:

$$V_{\text{LSR}} = V_{\text{Helio}} + (V_{\odot} \sin l + U_{\odot} \cos l) \cos b + W_{\odot} \sin b, \quad (1)$$

where l and b are the Galactic longitude and latitude, respectively, and U_{\odot} , V_{\odot} , and W_{\odot} denote the solar motion components in the direction of the Galactic Center, along Galactic rotation, and toward the north Galactic pole, respectively. The used values for U_{\odot} , V_{\odot} , and W_{\odot} are 10.3, 15.3, and 7.7 km s⁻¹, respectively (Kerr & Lynden-Bell 1986).

3. RESULTS

In the following we present the relationship between the molecular gas and YSOs in Section 3.1. Then, the distance to the S Mon region is estimated in Section 3.2 using YSOs that are closely correlated to the gas. In Section 3.3, we present the bubble observed in the S Mon region. An outflow is detected in one of clumps, as described in Section 3.4.

3.1. Relationship between the Molecular Gas and YSOs

Figure 1 shows a position–velocity (P-V) diagram (a) and the normalized V_{LSR} distribution (b) for YSOs and molecular gas traced by ¹²CO in S Mon. The ¹²CO emission shows two velocity components in this region, with one ranging from 0 to 7 km s⁻¹ and the other from 7 to 15 km s⁻¹. The presence of a gap or minimum in the CO emission at $V_{\text{LSR}} \sim 7$ km s⁻¹ is in agreement with the results of Tobin et al. (2015). In panel (b) of Figure 1, the V_{LSR} of the majority (62%) of the Class II YSOs peak at about 10 km s⁻¹, which is consistent with the ¹²CO emission component ranging from 7 to 15 km s⁻¹. Most (71%) Class III YSOs have LSR velocities between 0 and 7 km s⁻¹, with a peak at 5 km s⁻¹.

We investigate the two velocity components of molecular gas in S Mon separately. Figure 2 shows integrated maps of ¹²CO and HCO⁺ within the velocity range from 0 to 7 km s⁻¹ (panels (a) and (b)) and from 7 to 15 km s⁻¹ (panels (c) and (d)). The integrated map of molecular gas is superposed on a *Herschel* (Pilbratt et al. 2010) H₂ column density map of this region, with a resolution of 18'' (Nony et al. 2021). The ¹²CO and HCO⁺ emission between 0 and 7 km s⁻¹ appears to be diffuse and is not consistent with the *Herschel* H₂ column density map. This component seems to dominate in the easternmost area of the region. In particular in the ¹²CO map (Figure 2 (a)) there appears to be a somewhat stronger component starting from the left of the image, beyond the shown sky cutout. Our investigation does not include the easternmost region. The ¹²CO and HCO⁺ emission between 7 and 15 km s⁻¹ shows an arc-like structure, possibly indicative of a “bubble” (centered at (0, 0) offset, see more details in Section 3.3). We note that the distribution of the molecular gas within this velocity range is in agreement with the distribution of the *Herschel* H₂ column density map.

Figure 3 depicts the projected distribution of the YSOs in combination with ¹²CO emission and *Herschel* H₂ column density map. Both the Class II and Class III YSOs, which have LSR velocities between 7 and 15 km s⁻¹ (yellow pluses), generally coincide with the denser regions of the molecular cloud. More members associated with the molecular gas are found belong to the Class II YSOs.

Compared with the Class III YSOs, the Class II YSOs are better correlated with the molecular gas in both spatial distribution and kinematic properties. Considering the association between the molecular gas and the Class II YSOs, we are able to use the Class II YSOs to characterize the properties of the molecular gas, such as its distance and kinematics. The proper motions of the YSOs are used to derive the kinematics of the molecular gas in the plane of the sky, since they are the missing part, and cannot be measured directly for clouds.

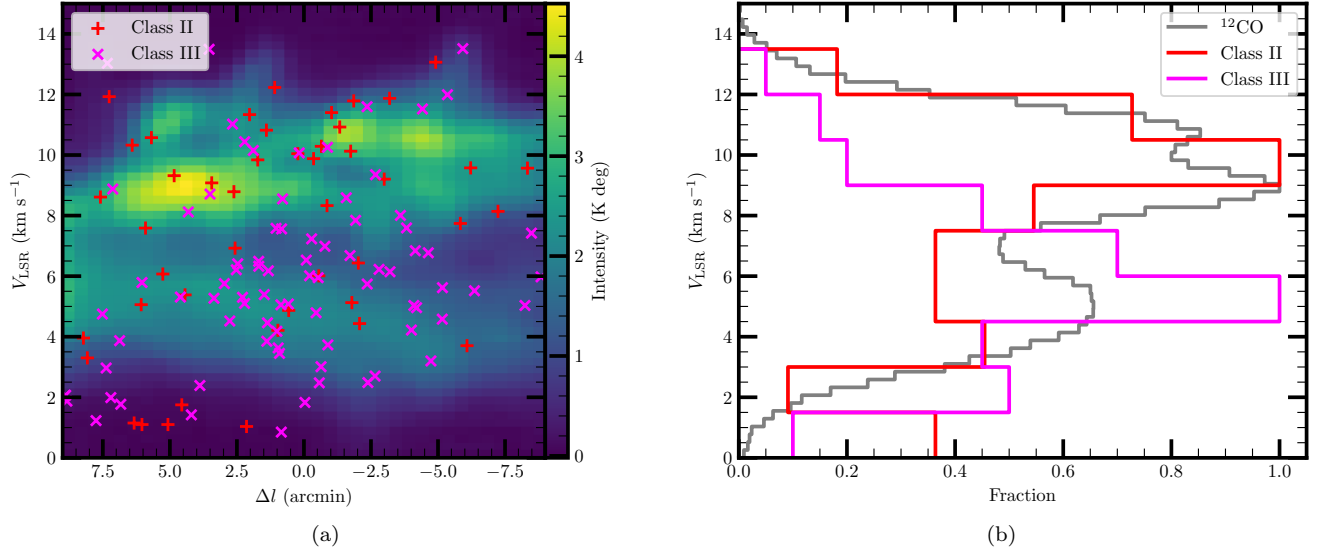


Figure 1. (a) P-V diagram showing ^{12}CO (background), Class II (red pluses), and Class III (magenta crosses) YSOs in S Mon. (b) Normalized histogram of V_{LSR} for ^{12}CO (gray line), Class II (magenta line), and Class III (red line) YSOs.

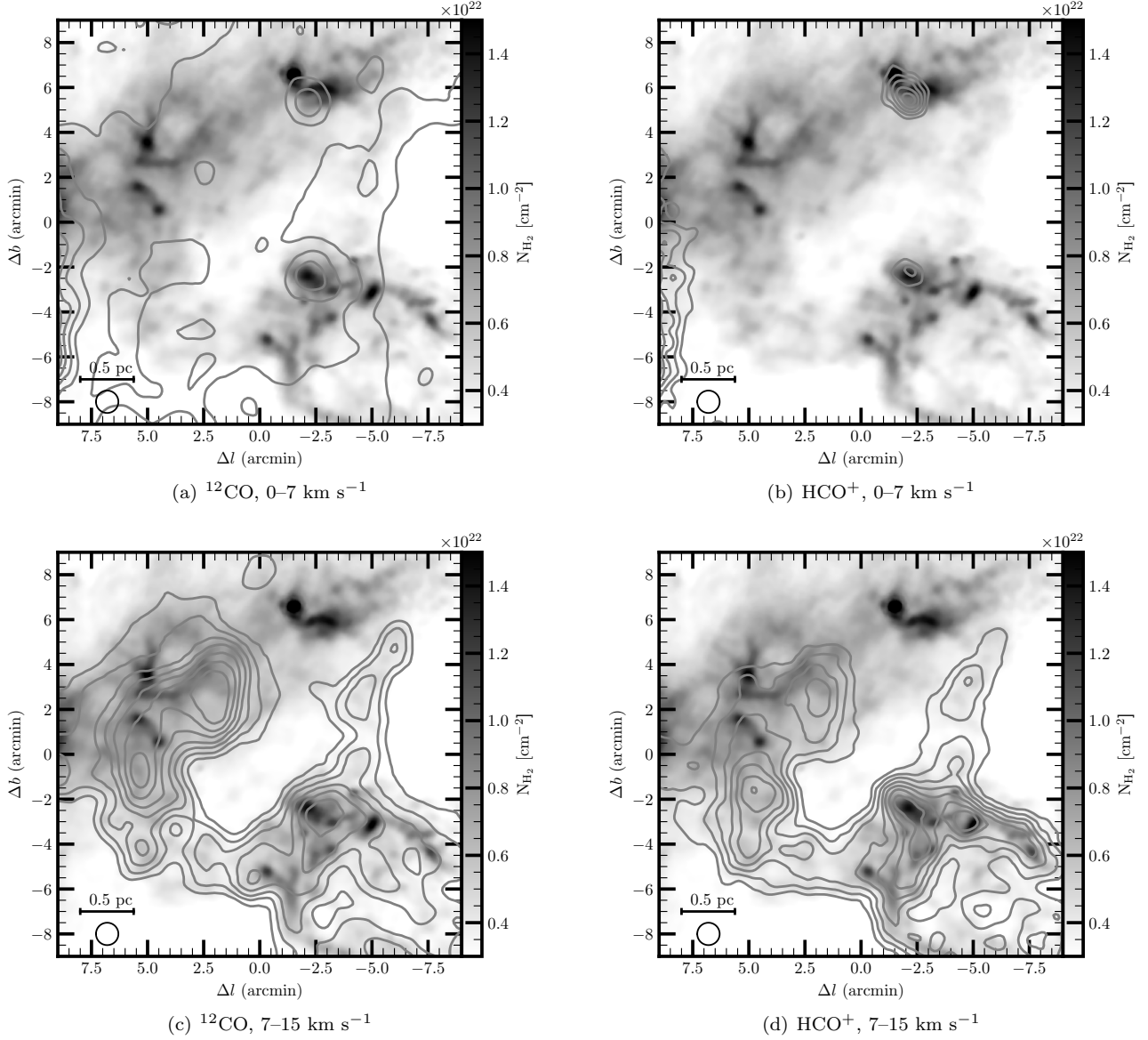


Figure 2. Integrated maps of ^{12}CO and HCO^+ over the velocity ranges of 0 to 7 km s^{-1} and 7 to 15 km s^{-1} . The contour levels are shown from 30% to 90% with steps of 10% of the peak integrated intensity, and the black open circle in the lower left corner of each panel represents the beam size of PMODLH. The gray background shows the *Herschel* H_2 column density map (Nony et al. 2021). In all panels, the (0, 0) offsets corresponds to $(l, b) = (202.95^\circ, 2.15^\circ)$.

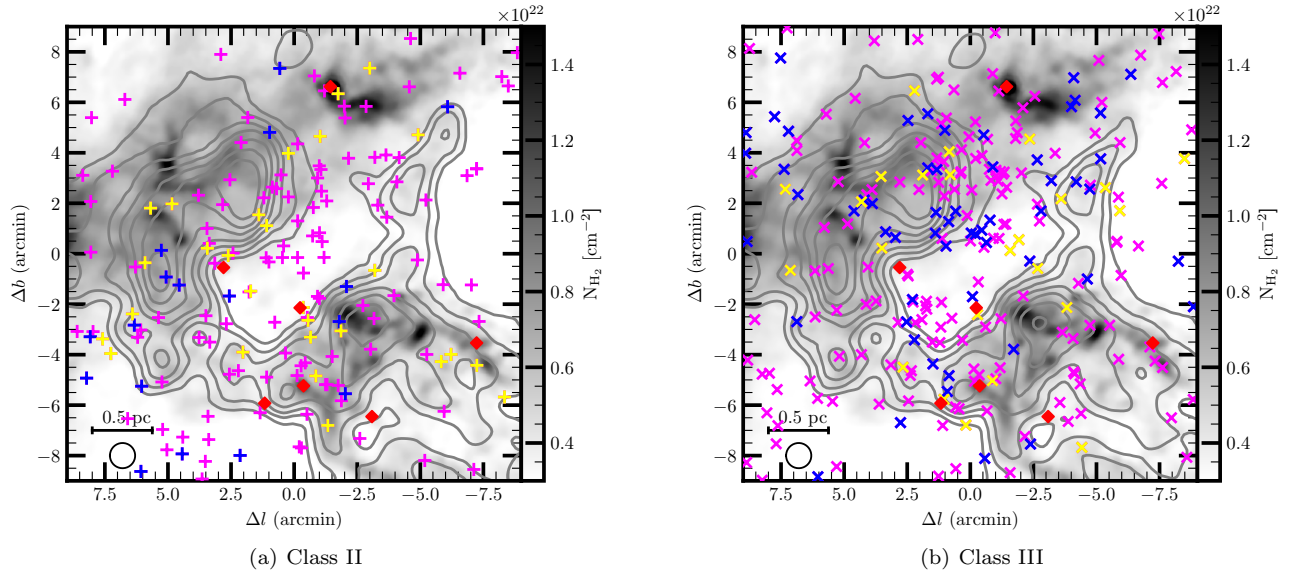


Figure 3. Projected distribution of Class II (left) and Class III (right) YSOs with different velocity ranges. The blue pluses (crosses) indicate Class II (III) YSOs with V_{LSR} ranging from 0 to 7 km s $^{-1}$. The yellow pluses (crosses) indicate Class II (III) YSOs with V_{LSR} ranging from 7 to 15 km s $^{-1}$. The magenta pluses (crosses) represent Class II (III) YSOs with unknown V_{LSR} . The red diamonds represent Class I YSOs. The gray contours and background are the same as in Figure 2.

3.2. Distance to S Mon

Accurate distances to molecular clouds are essential to study their physical properties. We employ the *Gaia* DR3 parallaxes of the Class II YSOs to estimate the distance to S Mon. In this work, only Class II YSOs with parallax accuracies better than 10% are selected for distance estimation. First, outliers of parallaxes beyond 3σ from the median value are excluded. Class II YSOs, which do not coincide with the gas distribution (CO at 7–15 km s⁻¹, magenta pluses in Figure 4 (a)), are also excluded from the distance estimation. Finally, a total 35 YSOs that meet these criteria are selected to estimate the distances shown (yellow pluses in Figure 4 (a)).

The distance is determined from *Gaia* parallaxes with $d(\text{pc}) = 1000/\varpi$, where ϖ is the parallax in units of mas. Lindegren et al. (2021) provided a method to correct the parallax zero points, however for red sources with $m_{G_{\text{BP}}} - m_{G_{\text{RP}}} > 1.6$, the correction could lead to a large parallax bias of about 40 μas . Since the photometric data of the used Class II YSOs have generally redder colors, we do not apply the parallax zero-point correction in this work.

We estimate the distance to the cloud directly using the YSOs associated with the cloud and their *Gaia* DR3 parallaxes. The cumulative distribution function (CDF) of *Gaia* distances is shown in panel (b) of Figure 4, where the median distance estimate is of 722 ± 9 pc. The uncertainty is derived by σ/\sqrt{N} , where σ represents the dispersion of the distance, and N represents the number of stars.

Flaccomio et al. (2023) conducted a study on the NGC 2264 star-forming region using X-ray data obtained with *XMM-Newton* telescope. The S Mon core region in their study appears to be close to the region we studied, although we note that they did not give the specific coordinates of the region they investigated. Although only half of the samples we used for distance estimation aligned with their sample counterparts, our distance estimation is similar to their results (719 ± 9 pc). However, the distance we derive is smaller than the distance estimated ($759_{-26}^{+10} \pm 37$ pc) by Zucker et al. (2020), who inferred the distance by fitting a line-of-sight dust model with *Gaia* DR2 data. We conducted a parallax difference test between *Gaia* DR2 and DR3 using a selected set of Class II YSOs in our region. These YSOs have LSR velocities ranging from 0 to 15 km s⁻¹, and both DR2 and DR3 exhibit parallax accuracies better than 10%. The difference between these two groups is approximately 25 pc, meaning the two estimates agree within their given uncertainties. Although we did not test the method of Zucker et al. (2020) explicitly, variations in methods could also introduce some differences in distance estimations. Therefore, the difference in distance between this work and that of Zucker et al. (2020) could be caused by the difference in both method and data. In the subsequent analysis, we adopt 722 ± 9 pc as the distance to the S Mon cloud, which has a velocity ranging between 7 and 15 km s⁻¹.

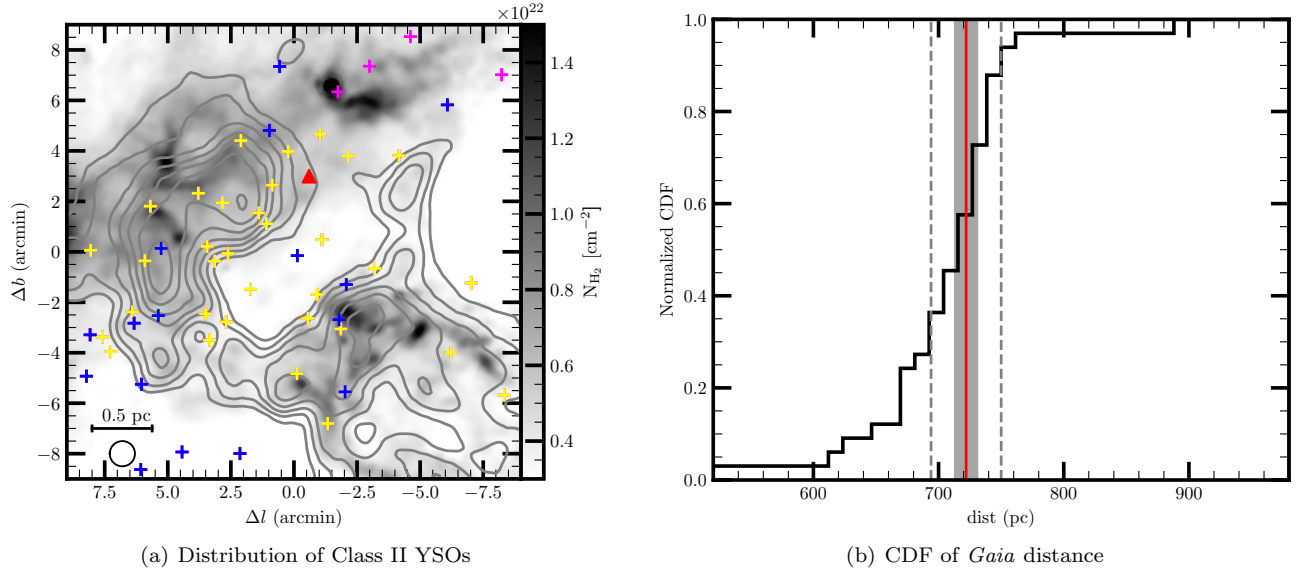


Figure 4. (a) Projected distribution of Class II YSOs with parallax uncertainties smaller than 10%. The yellow pluses are the Class II YSOs used for the distance estimation. The blue pluses show YSOs with LSR velocities smaller than 7 km s^{-1} . The magenta pluses show YSOs which do not coincide with the gas distribution. The red triangle represents the projected position of 15 Mon. (b) CDF of *Gaia* distances. The red vertical line indicates the median value of 722 pc, with a standard error of 9 pc denoted by the gray shadow. The upper and lower percentiles within 1σ around the median are labeled by the dashed gray lines.

3.3. Bubble

We identified the bubble in S Mon based on four criteria summarized from previous studies (e.g., Arce et al. 2011; Li et al. 2015; Feddersen et al. 2018): (1) the shell shows a circular or arc-like structure in integrated CO or HCO⁺ maps; (2) the P-V diagram of the shell shows an expansion signature (i.e., a “U” or “V” shape); (3) the CO or HCO⁺ shell matches the morphology of infrared data in at least one band; and (4) the shell contains a candidate driving source. An expanding bubble model requires three parameters: bubble radius (R_{bub}), expansion velocity (V_{exp}), and central velocity (V_{cnt}). We followed the method of Arce et al. (2011) to estimate these parameters. The radius is determined by a Gaussian fit to the azimuthally averaged profile of the integrated intensity map. The central and expansion velocities can be roughly read from a P-V diagram, where the upper part of the “U” or “V” structure corresponds to the central velocity and the difference between the central velocity and the lowest point of “U” or “V” structure indicates the expansion velocity. Then, the central and expansion velocities are corrected by visual fitting based on the channel maps. As indicated by Arce et al. (2011), the uncertainty in the central velocity of a bubble is about $\pm 0.5 \text{ km s}^{-1}$, and since the bubble is not detected over its entire velocity range, the expansion velocity is obtained as a lower limit.

An arc-like structure is clearly visible in the channel maps of ¹²CO and HCO⁺ (see the details in Figures 5–6), spanning a broad V_{LSR} range from 7.5 to 12.5 km s⁻¹. This structure is also evident in the integrated maps of ¹²CO and HCO⁺ from 7.5 to 12.5 km s⁻¹ and the *Herschel* H₂ column density map (see panels (a) and (d) of Figure 7, Nony et al. 2021). The P-V diagrams of ¹²CO and HCO⁺ (panels (b) and (e) of Figure 7) both show an upside down “U” or “V” shape. Based on the P-V diagram of ¹²CO (HCO⁺), V_{exp} and V_{cnt} are derived as $\sim 3.1 \text{ km s}^{-1}$ ($\sim 3.4 \text{ km s}^{-1}$) and $\sim 8.2 \text{ km s}^{-1}$ ($\sim 8.4 \text{ km s}^{-1}$), respectively. The V_{exp} values estimated from ¹²CO and HCO⁺ are similar, thus an average of 3.3 km s⁻¹ is adopted as a lower limit for the expansion velocity. The center of the bubble is set to be (0, 0). The radius and thickness of the bubble traced by the ¹²CO emission (see panel (c) of Figure 7) are ~ 5.4 and ~ 4.2 arcmin, respectively, corresponding to 1.13 and 0.88 pc at a distance of 722 pc. These values are compared with the bubble traced by HCO⁺ emission (see panel (f) of Figure 7), i.e., a radius of ~ 5.3 arcmin (~ 1.11 pc) and a thickness of ~ 4.4 arcmin (~ 0.92 pc). Based on both the ¹²CO and HCO⁺ emission and considering the uncertainties from the distance and the Gaussian fits, we derive the radius and thickness of the bubble to be 1.1 ± 0.1 pc and 0.9 ± 0.1 pc, respectively. The mean column density of the bubble is $\sim 2.5 \times 10^{20} \text{ cm}^{-2}$ and the mass (M_{shell}) is $\sim 1400 \pm 400 M_{\odot}$ (see the calculation and estimation of uncertainties in Appendix B).

Another arc-like structure appears to be located in the southwest region of the *Herschel* H₂ column density map (see the boxed region of Figure 8 (a)). The low-sensitivity CO data, observed using PMODLH, were employed to investigate the structure. The rms noise of the ¹²CO, ¹³CO and C¹⁸O spectra is 0.37, 0.20, and 0.20 K, respectively. A small arc-like structure is only evident in the ¹³CO integrated map (see panel (b) of Figure 8), so we use the ¹³CO data to produce a P-V diagram for the arc-like structure. However, there is no clear “U” or “V” shape in the P-V diagram (see panel (c) of Figure 8). In addition, we do not find a potential driving source for this arc-like structure. Moreover, using high-spatial-resolution CO maps (20”), Tauber et al. (1993) found that the properties of the northern region of the arc-like structure ($\Delta b > -7'$) are consistent with the ionizing radiation from 15 Mon, while those of the southern region are not. In conclusion, the arc-like structure shown is unlikely to be a bubble. Given the wind-blown appearance, this feature might be caused by feedback from the northeast side, coincident with the general location of the massive O- and B-type stars in the region.

There are eight clumps, labeled as A–H in Figure 7, identified from the integrated map of C¹⁸O emission. Figure 9 plots the four molecular lines we observed toward the C¹⁸O peak position of each clump. Table 2 lists the fits for the C¹⁸O peak emission for each clump. There are three main components among these eight clumps, i.e., $3 \text{ km s}^{-1} < V_{\text{LSR}} < 7 \text{ km s}^{-1}$, $7 \text{ km s}^{-1} < V_{\text{LSR}} < 10 \text{ km s}^{-1}$, and $10 \text{ km s}^{-1} < V_{\text{LSR}} < 13 \text{ km s}^{-1}$. As discussed in Section 3.1, the bubble is not associated with the component of $3 \text{ km s}^{-1} < V_{\text{LSR}} < 7 \text{ km s}^{-1}$, but instead with the other two components. Clumps A to D correlate with the velocity component of $7 \text{ km s}^{-1} < V_{\text{LSR}} < 10 \text{ km s}^{-1}$ and centered at $\sim 8.5 \text{ km s}^{-1}$, and clumps E to H correlate with the velocity component of $10 \text{ km s}^{-1} < V_{\text{LSR}} < 13 \text{ km s}^{-1}$ and centered at $\sim 10.5 \text{ km s}^{-1}$. Figure 10 shows integrated maps of C¹⁸O with different velocity components, which are in agreement with the parameters given in Table 2. These two groups of clumps correspond to different lobes of the bubble, so the different kinematic characteristics may be caused by the expansion of the bubble. Furthermore, the velocity dispersion around the bubble is larger (see Figure 11), indicating possible interaction between the bubble and surrounding gas. Table 3 lists the H₂ column density, mass, and turbulent energy of each clump derived using the optically thin ¹³CO line at the peak of the clump (see the calculations in Appendix B).

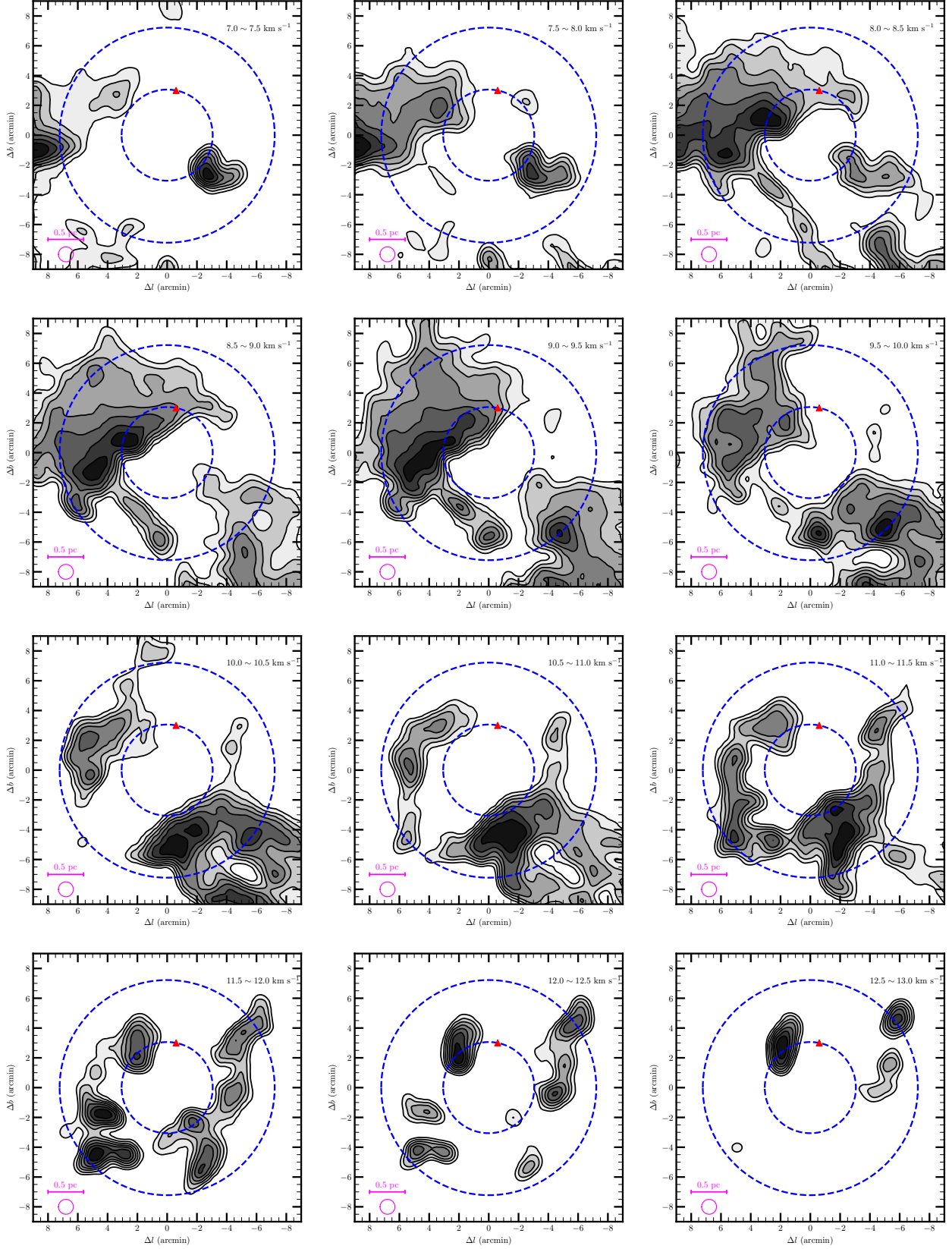


Figure 5. Channel maps of ^{12}CO emission. The red triangle represents the star 15 Mon. The blue dashed circle shows the bubble obtained by fitting the gas, which has a radius and thickness of ~ 5.4 and ~ 4.2 arcmin, respectively. The magenta circle indicates the beam size of PMODLH. The velocity range for each map is labeled in the upper right of the map.

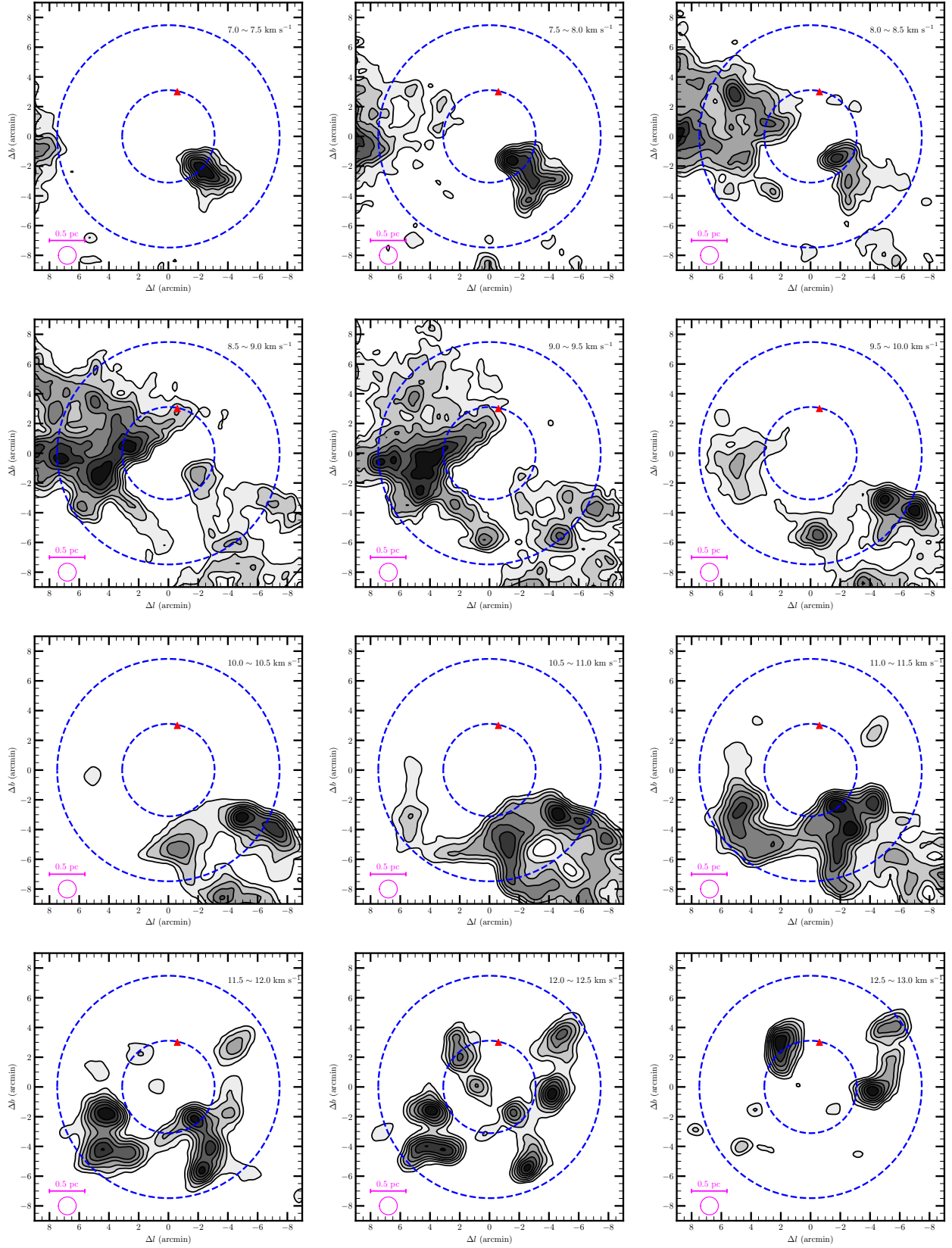


Figure 6. Channel maps of HCO^+ . The blue dashed circle shows the bubble obtained by fitting the gas, which has a radius and thickness of ~ 5.3 and ~ 4.4 arcmin, respectively. The other labels and colors are the same as in Figure 5.

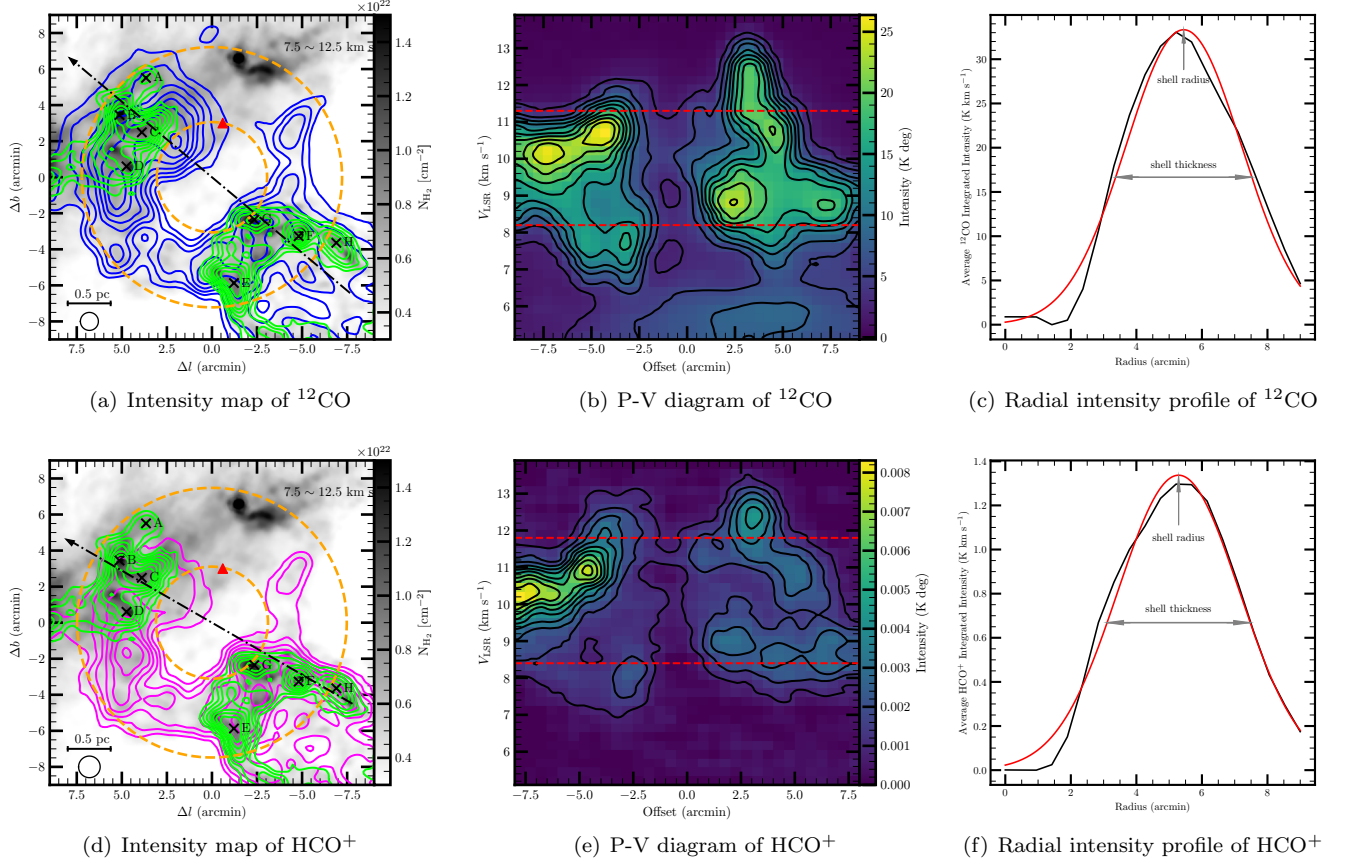


Figure 7. (a) Integrated map of ^{12}CO emission (blue contours) superposed on the *Herschel* H_2 column density map (gray background, Nony et al. 2021), and the green contour lines are the emission of C^{18}O . The integrated velocity range is $7.5 - 12.5 \text{ km s}^{-1}$ for both ^{12}CO and C^{18}O , and the contour levels are shown from 30% to 90% with steps of 10% of the peak integrated intensity of the corresponding emission. The orange dashed circle shows the bubble. Clumps identified based on the C^{18}O integrated map are labeled A to H. (b) P-V diagram of ^{12}CO along the arrow in panel (a), where the contour levels are shown from 10% to 90% with steps of 10% of the peak value. The red dashed lines show the expansion velocity range from the visual inspection, i.e., $8.2 - 11.3 \text{ km s}^{-1}$. (c) Azimuthally averaged radial intensity profile of the ^{12}CO bubble (black curve), where a Gaussian fit (red curve) to the intensity profile was performed to estimate the radius (peak) and thickness (Full Width at Half Maximum, FWHM). (d) Integrated map of HCO^+ (magenta contours). The other labels are the same as in panel (a). (e) P-V diagram of HCO^+ along the arrow in panel (d), and the expansion velocity range is $8.4 - 11.8 \text{ km s}^{-1}$. The other features are the same as in panel (b). (f) Azimuthally averaged radial intensity profile of the HCO^+ bubble, where the other labels and symbols are the same as in panel (c).

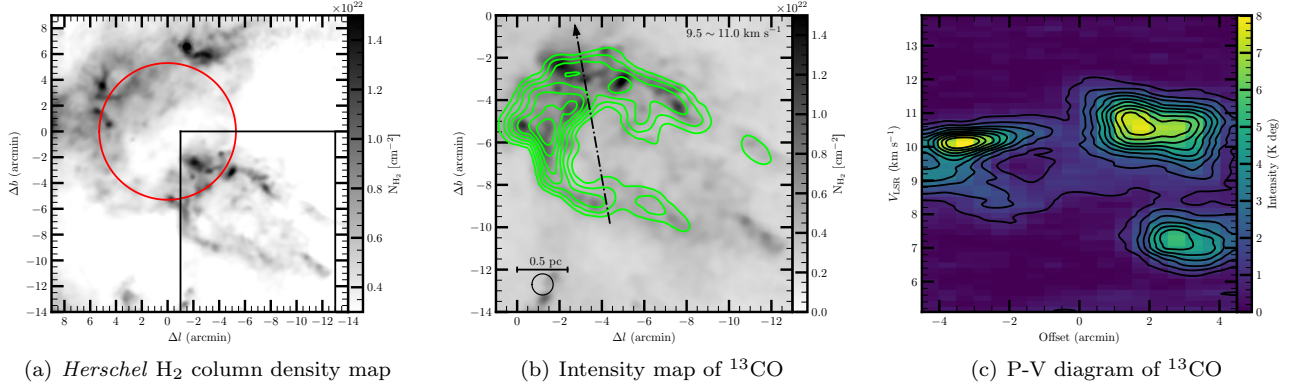


Figure 8. (a) *Herschel* H_2 column density map, showing a larger area to the southwest of the investigated region (Nony et al. 2021). The red circle depicts the bubble we identified, and the black box shows the region housing the small arc-like structure. (b) Integrated map of ^{13}CO emission (green contours) in the boxed region in panel (a). The integrated velocity range is $9.5 - 11.0 \text{ km s}^{-1}$, and the contour levels are shown from 30% to 90% with steps of 10% of the peak integrated intensity of ^{13}CO emission. (c) P-V diagram of ^{13}CO along the arrow in panel (b), where the contour levels are shown from 10% to 90% with steps of 10% of the peak integrated intensity of the corresponding emission.

Table 2. Observed Parameters of Each Clump

Clump	$^{12}\text{CO}(J = 1-0)$			$^{13}\text{CO}(J = 1-0)$			$\text{C}^{18}\text{O}(J = 1-0)$			$\text{HCO}^+(J = 1-0)$		
	T_{R}^* (K)	FWHM (km s^{-1})	V_{LSR} (km s^{-1})	T_{R}^* (K)	FWHM (km s^{-1})	V_{LSR} (km s^{-1})	T_{R}^* (K)	FWHM (km s^{-1})	V_{LSR} (km s^{-1})	T_{R}^* (K)	FWHM (km s^{-1})	V_{LSR} (km s^{-1})
(1)	(2)	(3)	(4)	(5)	(6)	(7)	(8)	(9)	(10)	(11)	(12)	(13)
A	19.1	2.5	9.1	6.5	1.5	9.2	2.1	0.4	9.2	0.4	2.6	9.2
B	17.9	3.3	8.7	6.0	2.3	8.6	2.1	0.8	8.7	0.6	2.1	8.5
C	19.5	3.3	8.5	8.1	1.7	8.2	2.7	0.6	8.3	0.6	1.8	8.3
D	26.1	3.0	8.8	6.9	1.9	9.0	2.3	0.4	9.2	0.7	2.9	9.0
E	29.7	2.8	10.6	10.8	1.7	10.6	2.7	0.6	10.6	1.9	2.5	10.8
F	25.3	2.0	10.5	7.6	1.7	10.3	1.9	0.6	10.2	2.3	1.9	10.4
G	26.5	2.6	10.8	7.7	2.0	10.8	1.6	0.7	10.8	1.7	2.4	11.1
H	23.1	2.9	9.8	6.7	1.9	9.9	1.5	0.5	10.1	1.8	1.9	10.3

NOTE—(1) Source name. (2), (5), (8), (11) Brightness temperature(s) of ^{12}CO , ^{13}CO , C^{18}O , and HCO^+ , respectively, at the emission peak of C^{18}O . (3), (6), (9), (12) FWHM of ^{12}CO , ^{13}CO , C^{18}O , and HCO^+ , respectively. (4), (7), (10), (13) Central velocity of ^{12}CO , ^{13}CO , C^{18}O , and HCO^+ , respectively.

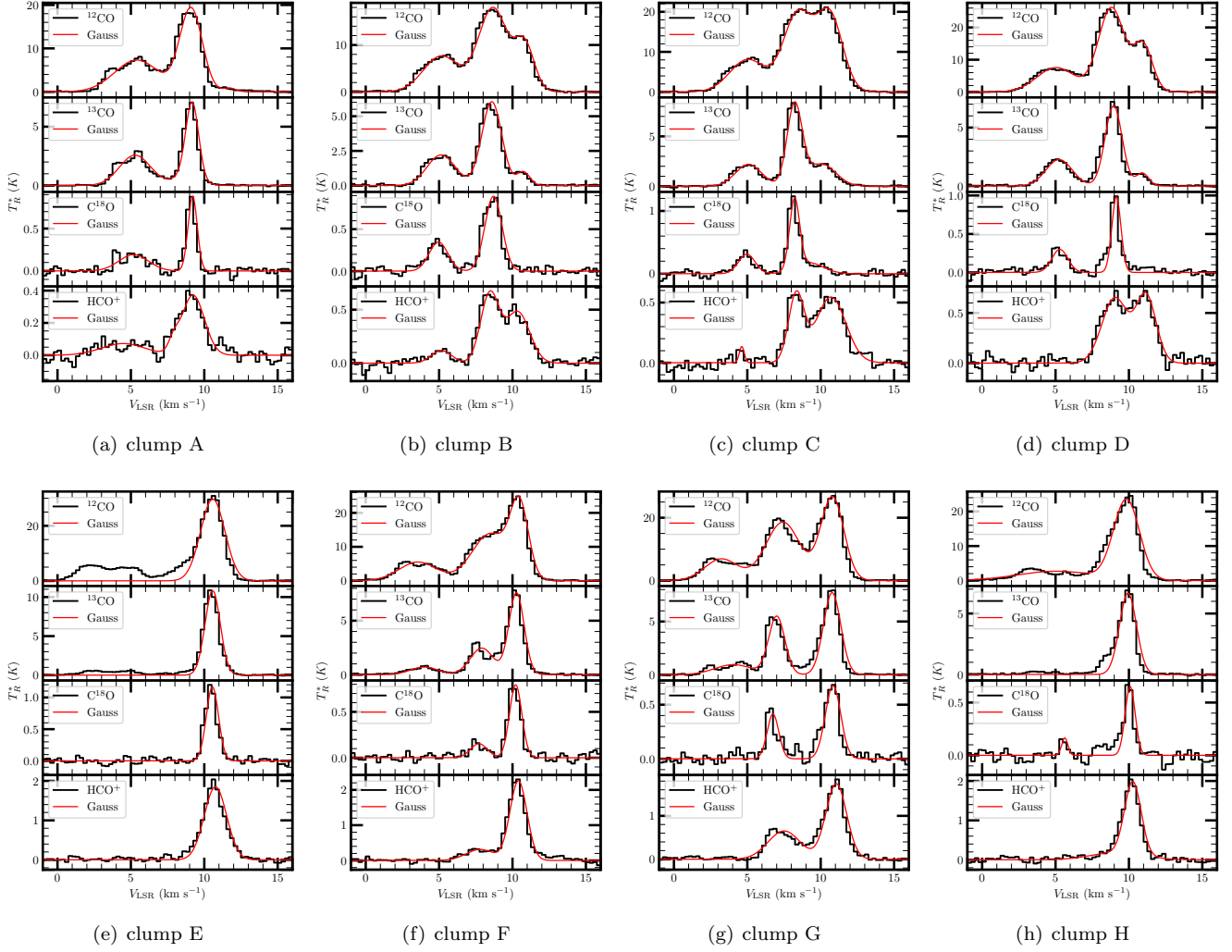


Figure 9. Spectra of ^{12}CO , ^{13}CO , C^{18}O , and HCO^+ of the C^{18}O peak position of clumps A to H. The red lines represent the sum of the multiple Gaussian fitting components.

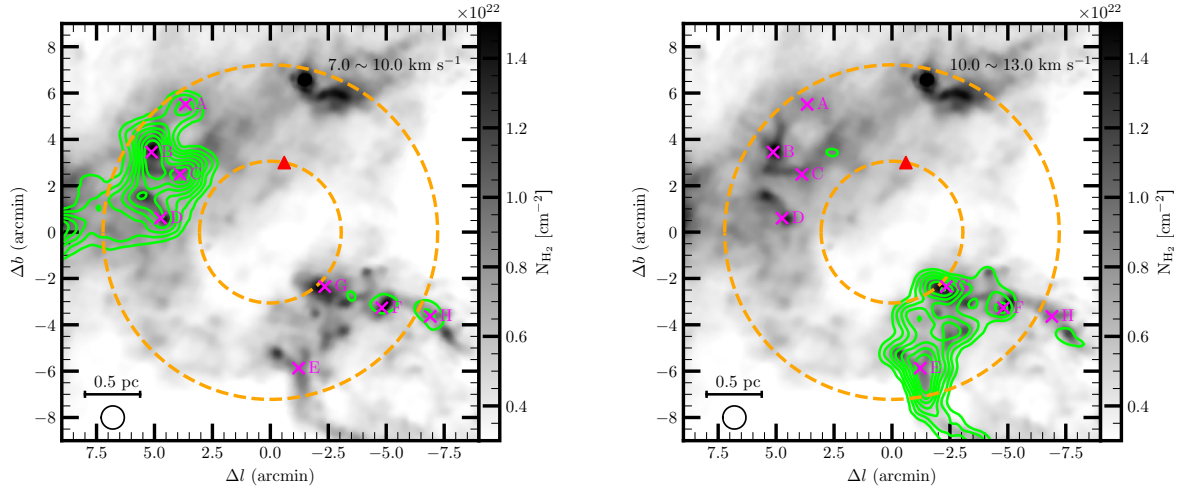


Figure 10. Integrated map of C^{18}O superposed on the *Herschel* column density map. The velocity range for the left panel is $7\text{--}10 \text{ km s}^{-1}$, and for the right panel is $10\text{--}13 \text{ km s}^{-1}$. The other features are the same as in Figure 7 (a).

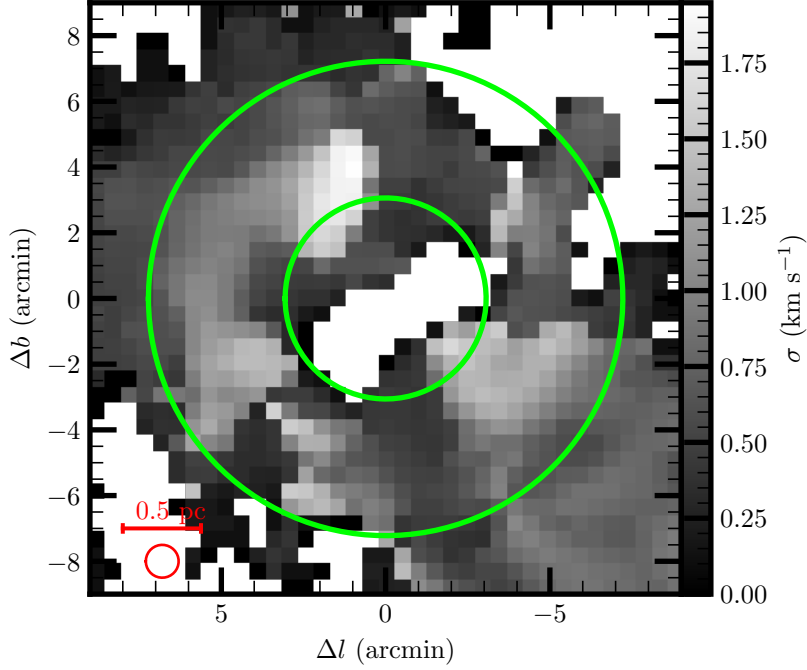


Figure 11. Distribution of the velocity dispersion (σ). The green circles indicate the bubble region.

Table 3. Physical Parameters of the Clumps

Clump	T_{ex} (K)	d_{clump} (pc)	$\int T_{\text{mb},13} dv$ (K km s $^{-1}$)	$N_{\text{H}_2, \text{clump}}$ (10^{20} cm $^{-2}$)	M_{clump} (M_{\odot})	$E_{\text{turb, clump}}$ (10^{44} erg)	$E_{\text{grav, clump}}$ (10^{43} erg)
(1)	(2)	(3)	(4)	(5)	(6)	(7)	(8)
A	22.6	0.2 ± 0.1	15.4	2.7	8.1 ± 2.1	1.3 ± 0.3	5.6 ± 0.8
B	21.3	0.2 ± 0.1	16.5	2.4	5.8 ± 2.0	2.2 ± 0.8	2.9 ± 0.7
C	23.0	0.3 ± 0.1	20.5	3.7	14.3 ± 3.6	3.0 ± 0.8	11.7 ± 2.2
D	29.6	0.3 ± 0.1	16.2	3.4	10.4 ± 2.7	2.7 ± 0.7	6.2 ± 1.2
E	33.2	0.5 ± 0.1	16.8	6.1	24.8 ± 5.1	5.2 ± 1.1	21.0 ± 4.4
F	28.8	0.4 ± 0.1	16.1	3.7	11.5 ± 3.0	2.4 ± 0.6	5.7 ± 1.5
G	30.0	0.5 ± 0.1	22.6	3.9	16.7 ± 4.2	4.9 ± 1.2	9.5 ± 3.0
H	26.6	0.6 ± 0.1	10.5	3.1	7.7 ± 1.7	2.0 ± 0.4	1.7 ± 0.5

NOTE—(1) Source name. (2) Excitation temperature of the clump, which is obtained by the ^{12}CO spectral line from the C^{18}O peak emission of each clump. (3) Diameter of the clump. (4) Integrated intensity of ^{13}CO emission. (5) H_2 density of the clump. (6) Mass of the clump. (7) Turbulent energy of the clump. (8) Gravitational energy of the clump.

3.4. The outflow of clump E

In this section we investigate clump E in more detail, since the velocity profile of this clump alone displays typical outflow characteristics and because the spectra of the other clumps are too complex to identify reliable outflows. Outflows are a direct signature of ongoing star formation, and they can be identified by examining their line profiles, integrated intensity maps, and P-V diagrams. The central velocity and position of the driving source are estimated through the C^{18}O line. The emission peaks of C^{18}O can be seen in Figure 7. The initial velocity ranges of the blue and red wings are determined from the line wings of the spectral line where the C^{18}O emission reaches the 1σ noise level. According to morphologies of the P-V diagram and the integrated map of the line wings of the ^{13}CO and HCO^+ emission, then visually adjusted the velocity range of the line wings. To improve the signal-to-noise ratio, we smooth the CO and HCO^+ lines to a velocity resolution of 0.25 km s^{-1} .

Figures 12 and 13 show the identified outflow in clump E based on ^{13}CO and HCO^+ emission, respectively. The spatial distributions of the ^{13}CO and HCO^+ outflows are consistent with each other and are aligned along the east–west direction. The blue and red lobes are symmetrically distributed with respect to the C^{18}O emission peak, which are similar in size. We note that the C^{18}O and HCO^+ emission at $V_{\text{LSR}} \sim 8.6 \text{ km s}^{-1}$, and the offset of ~ 1.5 arcmin in the P-V diagram, are not associated with the blue lobe of the outflow, thus we did not cut the edge of the blue wing to the 1σ noise level.

The method presented in Liu et al. (2021) was employed to estimate various properties of the outflows, such as the mass, momentum, and energy. Therein, they derived the H_2 column density of the outflow lobes assuming that the gas is in local thermodynamic equilibrium (LTE) and the excitation temperature is 30 K (15 K) for ^{13}CO (HCO^+). The mass of an outflow lobe can be then estimated based on its size and the H_2 column density. The other physical properties of the outflows are obtained based on the mass, velocity, and size of the lobes (see Appendix A of Liu et al. 2021). In our work, we use the ratios of column densities of $N_{\text{H}_2}/N_{^{13}\text{CO}} \approx 5 \times 10^5$ and $N_{\text{H}_2}/N_{\text{HCO}^+} \approx 10^8$ (Turner et al. 1997; Simon et al. 2001). We also use the inclination of the outflow, i.e., the angle between the long axis of the outflow and the line of sight, to correct the parameters of the outflow. Since the inclination of an outflow cannot be reliably determined, we adopt $57^\circ 3$ as a proxy in this work, which is the mean value for a random distribution (see details in Bontemps et al. 1996; Li et al. 2018). We note that the calculation of the outflow’s physical parameters (see Table 4), involve many assumptions, such as the excitation temperature and the inclination. Therefore, we only consider the uncertainties in the outflow lobe region and distance when estimating the errors of the physical parameters. The mass, momentum, and dynamical timescale of the outflow are a few M_\odot , a few tens of $M_\odot \text{ km s}^{-1}$, and $\sim 10^5 \text{ yr}$, respectively. Based on Yang et al. (2018), the typical mass of a low-mass outflow is about $0.1 \sim 1 M_\odot$ and the typical mass loss rate is about $10^{-7} \sim 10^{-6} M_\odot \text{ yr}^{-1}$. These values are much smaller than those found for the outflow in clump E. Moreover, all physical parameters of the outflow in clump E align with the typical values of high-mass outflows as summarized in table 1 of Yang et al. (2018). Therefore, it is unlikely that the outflow in clump E is driven by a single low-mass YSO. We do not find any high-mass YSOs in this region based on the current data, yet there are several low-mass YSOs embedded in the vicinity of the outflow region (see panel (a) of Figures 12 and 13). Therefore, the outflow might be driven by a deeply embedded protostar that has not been detected yet.

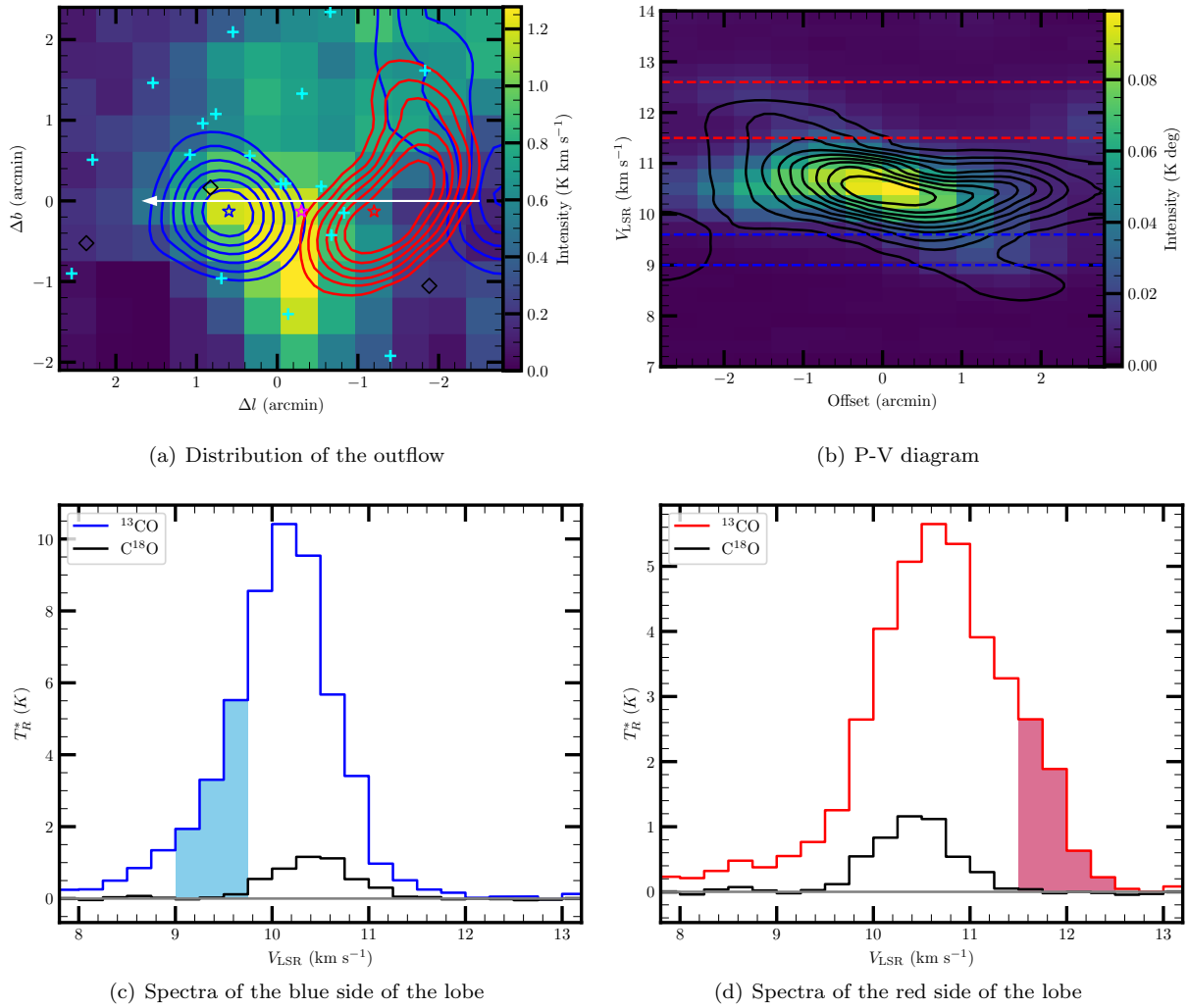


Figure 12. Outflow in clump E identified by ^{13}CO emission. (a) Integrated $C^{18}O$ map with ^{13}CO blue and red lobe contours. The contour levels are shown from 40% to 90% with steps of 10% of the peak intensity of each lobe. The black diamonds and cyan pluses represent Class I and Class II YSOs, respectively. The magenta, blue, and red stars are the emission peaks of $C^{18}O$, and the blue lobe and red lobe, respectively. (b) P-V diagram along the white arrow in panel (a). The black contour levels are shown from 10% to 90% with steps of 10% of the peak value. The blue and red dashed lines are the velocity ranges of the blue and red lobes, respectively. (c) The blue spectrum presents ^{13}CO at the peak position of the blue emission of the ^{13}CO outflow. The black spectrum is $C^{18}O$ at the emission peak of $C^{18}O$. The blue shading of the spectrum indicates the blue line wing velocity of ^{13}CO . The feature at 8.6 km s $^{-1}$ is likely unrelated to the outflow, so emission with a velocity below 8.6 km s $^{-1}$ is not included in the blue wing of the outflow profile. (d) The red spectrum is ^{13}CO at the peak position of the red emission of the ^{13}CO outflow. The black spectrum is $C^{18}O$ at the emission peak of $C^{18}O$. The red shading of the spectrum indicates the red line wing velocity of ^{13}CO .

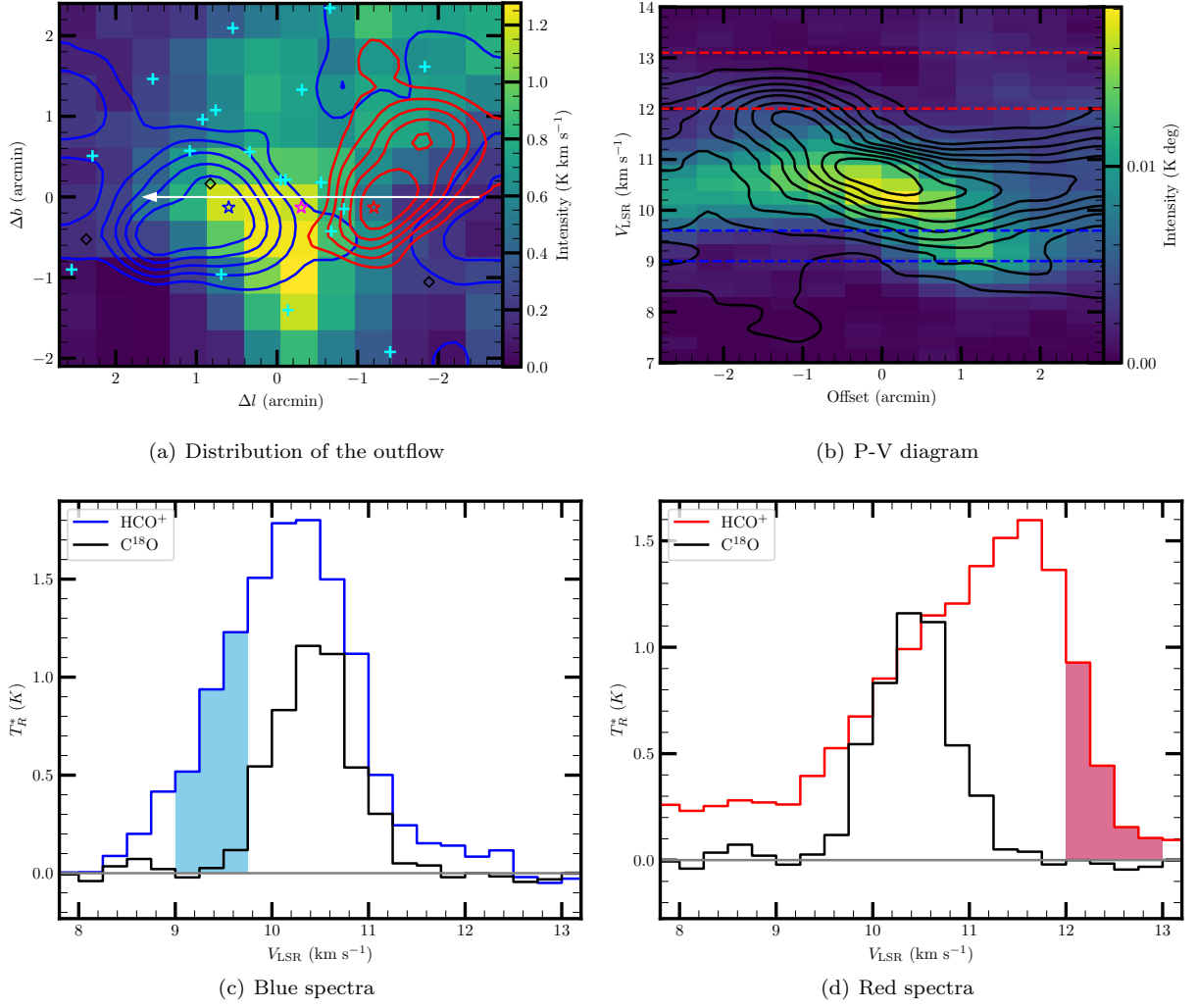


Figure 13. Outflow in clump E identified by HCO^+ emission. The description of each panel is the same as that in Figure 12, except the contour levels in panel (a) are shown from 50% to 90% with steps of 10% of the peak intensity of each lobe.

Table 4. Physical Properties of the Outflow of Clump E

Line	Lobe	Δv (km s ⁻¹)	$\langle \Delta v_{\text{lobe}} \rangle$ (km s ⁻¹)	N_{H_2} (10 ²¹ cm ⁻²)	M_{lobe} (M_{\odot})	l_{lobe} (pc)	P_{lobe} (M_{\odot} km s ⁻¹)	E_{lobe} (10 ⁴⁴ erg)	t_{lobe} (10 ⁵ yr)	$L_{\text{m (lobe)}}$ (10 ⁻¹ L_{\odot})
(1)	(2)	(3)	(4)	(5)	(6)	(7)	(8)	(9)	(10)	(11)
¹³ CO	blue	(9, 9.6)	2.1	1.1	6.2 ± 1.2	0.8 ± 0.2	24.6 ± 4.7	9.1 ± 1.8	2.2 ± 0.3	1.8 ± 0.2
¹³ CO	red	(11.5, 12.6)	2.7	1.1	9.6 ± 2.8	0.9 ± 0.2	49.8 ± 13.9	24.3 ± 6.4	2.0 ± 0.3	5.3 ± 0.6
HCO ⁺	blue	(9, 9.6)	2.1	0.4	2.5 ± 0.9	0.8 ± 0.1	10.1 ± 3.4	3.7 ± 1.3	2.3 ± 0.4	0.7 ± 0.1
HCO ⁺	red	(12, 13)	2.7	0.5	2.9 ± 0.6	0.8 ± 0.1	14.7 ± 3.3	7.1 ± 1.6	1.8 ± 0.2	1.8 ± 0.2

NOTE—(1) Molecular line. (2) Blue/red lobe. (3) Outflow velocity range for the blue/red lobe. (4) Velocity of the blue/red lobe. (5) H₂ density of the blue/red lobe. (6) Mass of the blue/red lobe. (7) Length of the blue/red lobe. (8) Momentum of the blue/red lobe. (9) Kinetic energy of the blue/red lobe. (10) Dynamical timescale of the blue/red lobe. (11) Mechanical luminosity of the blue/red lobe.

4. DISCUSSION

In this section, we discuss the physical properties of the bubble (Section 4.1), and the energy cascade of S Mon region (Section 4.2). In Section 4.3, we use the Class II YSOs to investigate the kinematic characteristics of the bubble.

4.1. Physical Properties of the Bubble

In the following, we discuss the physical properties of the bubble. Using the shell mass (M_{shell}) and expansion velocity (V_{exp}) of the bubble, we can estimate the shell's momentum (P_{shell}), kinetic energy (E_{shell}), and kinetic timescale (t_{kinetic}). These quantities are determined as $P_{\text{shell}} = M_{\text{shell}}V_{\text{exp}}$, $E_{\text{shell}} = 0.5M_{\text{shell}}V_{\text{exp}}^2$, and $t_{\text{kinetic}} = R_{\text{bub}}/V_{\text{exp}}$, respectively. For the bubble we find that P_{shell} is $4\,600 \pm 1\,300 M_{\odot} \text{ km s}^{-1}$, E_{shell} is $(1.5 \pm 0.4) \times 10^{47}$ erg, and t_{kinetic} is $(3.3 \pm 0.3) \times 10^5$ yr. Considering that the expansion velocity serves as a lower limit, the uncertainties of these parameters only come from the mass.

We find 13 B-type stars and a massive binary system, 15 Mon, located in the S Mon region using SIMBAD¹. Most B-type stars are located in the shell of the bubble rather than at its center (see Figure 19 in Appendix C), and only two B-type stars are located at the center of the bubble. We employ Equation (2) from Arce et al. (2011) to estimate the mass-loss rate (\dot{m}_{w}), which can be calculated by:

$$\dot{m}_{\text{w}} = \frac{P_{\text{shell}}}{v_{\text{w}}\tau_{\text{w}}}, \quad (2)$$

where v_{w} is the wind velocity, and τ_{w} is the wind timescale (i.e., the duration of wind activity). Here, the kinetic timescale (t_{kinetic}) is employed to estimate the mass-loss rate of the driving source roughly. Given the typical wind velocity of O- or B-type stars is about 1 000–2 000 km s⁻¹ (Chen et al. 2013), the mass-loss rate would be $10^{-6} - 10^{-5} M_{\odot} \text{ yr}^{-1}$. The value is much larger than the typical mass-loss rate of B-type stars ($10^{-8} - 10^{-11} M_{\odot} \text{ yr}^{-1}$) but close to that of O-type stars ($10^{-6} - 10^{-7} M_{\odot} \text{ yr}^{-1}$, Chen et al. 2013). Therefore, it is improbable that the B-type stars are the main driving source of the bubble. Although 15 Mon is not precisely at the center of the bubble, it stands out as the closest high-mass star to the bubble's center, apart from the two B-type stars. Therefore, 15 Mon might be the main driving source of the bubble.

The dynamic age of the H_{II} region can be used to judge whether the bubble is triggered by 15 Mon. Assuming that the H_{II} region expands in a homogeneous medium, its dynamical age, t_{dyn} is (see the model described by Dyson & Williams 1980):

$$t_{\text{dyn}} = \frac{4R_{\text{s}}}{7c_{\text{s}}} \left[\left(\frac{R_{\text{HII}}}{R_{\text{s}}} \right)^{7/4} - 1 \right], \quad (3)$$

where R_{HII} is the radius of the H_{II} region (Xu et al. 2017), for which we adopt an inner radius of 0.7 ± 0.1 pc. c_{s} is the isothermal sound speed of the ionized gas, and a value of 10 km s⁻¹ is adopted. The radius of the associated Strömrgren sphere (R_{s}) reads:

$$R_{\text{s}} = \left(\frac{3Q_{\text{Ly}}}{4\pi n_0^2 \alpha_B} \right)^{1/3}, \quad (4)$$

where $\alpha_B = 2.6 \times 10^{-13} \text{ cm}^3 \text{ s}^{-1}$ is the hydrogen recombination coefficient to all levels above the ground level, n_0 is the initial number density of the gas, and Q_{Ly} is the ionizing luminosity. We only consider the number of atoms that can be ionized, so $n_0 = \frac{M_{\text{shell}}}{4/3\pi R_{\text{pub}}^3} \approx (2.6-6.3) \times 10^4 \text{ cm}^{-3}$. Since the actual ionized medium within the bubble is likely less massive as compared to the whole shell mass determined from the broad CO ring, the number of atoms that can be ionized might be overestimated. For an O7V star, the ionizing luminosity (Q_{Ly}) is $10^{47.62} \text{ s}^{-1}$ (Martins et al. 2005). Based on these calculations, the obtained dynamical age is $(3.5-8.9) \times 10^5$ yr. Even if the secondary member of 15 Mon, an O9.5V star, is also taken into account, the dynamical timescale is only reduced by less than 0.1%. We conclude that the kinetic timescale of the bubble is comparable to the dynamical age of the H_{II} region.

Montillaud et al. (2019) estimated the age of 15 Mon using two methods. The first method, based on SED fitting, led to a median age of 1.5–2 Myr, with a dispersion between 0.2 and 3 Myr. The second method was based on isochrone

¹ <https://simbad.u-strasbg.fr/simbad>

fitting in color–magnitude diagrams and led to a median age of 3 Myr, with a dispersion between 1 and 6 Myr. Our estimation on the dynamical timescale of the H_{II} region may be less than the age of 15 Mon. Hence, the bubble is likely to be driven by the expanding H_{II} region of 15 Mon. As the projected position of 15 Mon is not located at the center of the bubble, we presume that 15 Mon may have moved away from its once central position in the bubble.

4.2. Energy Cascade in S Mon

Stellar winds inject energy and momentum into the ambient clouds that may help sustain turbulence and disrupt their surroundings (Nakamura & Li 2007; Arce et al. 2011). To assess whether winds can sustain the turbulence in S Mon, we compare the wind energy injection rate into the cloud, \dot{E}_w , with the cloud turbulent dissipation rate, $L_{\text{turb,cloud}}$. Based on the ¹³CO emission, we can derive the 3D turbulent velocity dispersion (σ_{3d}) with an approximation of $\sigma_{3d} = \sqrt{3}\sigma_{1d}$ (Li et al. 2018), where σ_{1d} is the 1D turbulent velocity dispersion along the line of sight and we consider the mass (M_{cloud}) of S Mon. The obtained σ_{3d} is $1.7 \pm 0.2 \text{ km s}^{-1}$ and M_{cloud} is $2\,200 \pm 500 M_{\odot}$. The cloud turbulent energy, $E_{\text{turb,cloud}}$, is about $(6.3 \pm 2.5) \times 10^{46} \text{ erg}$ (see the calculation in Appendix B). The cloud turbulent dissipation rate can be calculated as:

$$L_{\text{turb,cloud}} = \frac{E_{\text{turb,cloud}}}{t_{\text{diss}}}, \quad (5)$$

where t_{diss} is the cloud turbulent dissipation time. We roughly estimate t_{diss} via (McKee & Ostriker 2007):

$$t_{\text{diss}} \sim 0.5 \frac{d_{\text{cloud}}}{\sigma_{1d}}, \quad (6)$$

where the cloud diameter is $d_{\text{cloud}} \sim (4.0 \pm 0.4) \text{ pc}$ and $\sigma_{1d} \sim (1.0 \pm 0.1) \text{ km s}^{-1}$. Based on Equations (5)–(6), we obtain a cloud turbulent dissipation time of $t_{\text{diss}} \sim (2.0 \pm 0.4) \times 10^6 \text{ yr}$, and a cloud turbulent dissipation rate of $\sim (0.5\text{--}1.7) \times 10^{33} \text{ erg s}^{-1}$.

Since the bubble might be driven by the expanding H_{II} region of 15 Mon, the dynamical age (t_{dyn}) of the bubble is more suitable than the kinematic timescale (t_{kinetic}) to estimate the mass-loss rate (\dot{m}_w). Therefore, we reestimated this value, which is approximately $(1.9\text{--}8.6) \times 10^{-6} M_{\odot} \text{ yr}^{-1}$, and the wind energy injection rate can be estimated using the following equation from McKee (1989):

$$\dot{E}_w = \frac{1}{2} (\dot{m}_w v_w) \sigma_{3d}. \quad (7)$$

The derived wind injection rate is about $(4.5\text{--}8.1) \times 10^{33} \text{ erg s}^{-1}$, which is larger than the cloud turbulent dissipation rate. This indicates that strong winds serve as a significant energy origin for S Mon, consisting of sustaining the observed turbulence. This result agrees with the findings of other studies (Arce et al. 2011; Li et al. 2015; Feddersen et al. 2018).

In the following, we investigate the turbulent energy in this region. The total wind energy input into the interstellar medium is about $E_w = \int 0.5 \dot{m}_w(t) v_w^2 dt \simeq \Delta M v_w^2 / 2 \simeq (0.7\text{--}1.7) \times 10^{50} \text{ erg}$ (Lamers & Cassinelli 1999). Both the wind energy of 15 Mon and the kinetic energy of the bubble ($E_{\text{shell}} \sim (1.5 \pm 0.4) \times 10^{47} \text{ erg}$) are higher than the turbulent energy of the cloud ($E_{\text{turb,cloud}} \sim (6.3 \pm 2.5) \times 10^{46} \text{ erg}$), thus both of them are help to sustain the turbulence in the S Mon region. Moreover, the wind energy probably plays a crucial role in driving the bubble, since it is about three orders of magnitude higher than the kinetic energy of the bubble. Despite the substantial energy carried away by ionizing photons from the star throughout its lifetime, only 0.01–0.1 percent of this energy is converted into kinetic energy in the shell, with the majority being lost as radiation (Geen et al. 2015). Walch et al. (2012) conducted hydrodynamic simulations to explore the dynamical effects of a single O7 star. They determined that the total radiative energy injected by the ionizing source reaches $7 \times 10^{51} \text{ erg}$ within approximately 1 Myr. A portion of this injected energy is then transformed into kinetic energy, amounting to around $3 \times 10^{48} \text{ erg}$, which surpasses the kinetic energy we estimated in this work ($E_{\text{shell}} \sim (1.5 \pm 0.4) \times 10^{47} \text{ erg}$). Thus, radiative energy contributes to driving the bubble.

Next, we studied the turbulent energy of the outflow of clump E. The total kinetic energy of the outflow in clump E ($\sum E_{\text{lobe}} \sim 4.4 \times 10^{45} \text{ erg}$) is higher than its turbulent energy ($E_{\text{turb,clump}} \sim (5.2 \pm 1.1) \times 10^{44} \text{ erg}$), and it accounts for $\sum E_{\text{lobe}} / E_{\text{turb,cloud}} \sim 4\text{--}10\%$ of the turbulent energy of the cloud. This suggests that the outflow in clump E helps to maintain the turbulence in this clump and introduces additional energy to surrounding gas, thereby affecting the turbulence of the local environment (Arce et al. 2010; Li et al. 2018). This result is also consistent with the conclusion made by Li et al. (2020) that the outflow is sufficient to maintain turbulence on a scale of 0.1–0.4 pc.

Moreover, we also estimate the gravitational binding energy of the S Mon region. The detailed calculation is presented in Appendix B. We find that the total wind energy of 15 Mon is over two orders of magnitude higher than the gravitational binding energy of the cloud, i.e., $(2.1 \pm 1.0) \times 10^{47}$ erg, indicating that the wind can disrupt the cloud. Based on the above calculations, we find that half of the gravitational binding energy of the cloud is approximately equal to the kinetic energy of the bubble, and much higher than the total kinetic energy of the outflow in clump E. According to the virial theorem (Nakamura & Li 2014), the bubble has the potential to disrupt the cloud, while the outflow is unable to disrupt the cloud.

We also investigated the gravitational binding energy of clump E ($E_{\text{grav,clump}} \sim (2.1 \pm 0.2) \times 10^{44}$ erg), which is lower than the total kinetic energy of the outflow, indicating that the outflow contributes to disrupting the clump. The results for the outflow found here are consistent with the conclusions made by Li et al. (2020) in that the outflow activity could potentially disperse material away from the parent cloud on a scale of 0.2 – 1.0 pc.

In conclusion, we find the bubble produced by 15 Mon helps to maintain the turbulence in S Mon and is potentially disrupting the cloud, and while the outflow from clump E only adds a small fraction of the overall turbulence and energy of the system, it still may be able to perturb the local gas.

4.3. Bubble from the YSO Perspective

Since some YSOs may be too young to have moved away from their birth sites, they often have the same kinematic properties as their parent clouds (Tobin et al. 2015; Hacar et al. 2016; Großschedl et al. 2021). Thus, we can utilize the motions of YSOs associated with a cloud to represent the motions of the cloud. According to the correlation between YSOs and gas (see Section 3.1 for details), the Class II YSOs, whose parallax accuracies are better than 10% and projected locations are approximately aligned with the cloud were initially selected to investigate the kinematic characteristics of the bubble.

A Gaussian function was used to estimate the average proper motion of the YSO sample and to remove outliers (beyond a 3σ threshold). A total of 38 YSOs were ultimately selected to investigate the kinematic features of the bubble on the plane of the sky. Figure 14 (a) shows the distribution of proper motion of the selected YSOs. The mean proper motion of these sources is $(\bar{\mu}_l, \bar{\mu}_b) = (2.65, -3.17)$ mas yr⁻¹, and the 1σ uncertainty range of the Gaussian fitting is (0.14, 0.17) mas yr⁻¹.

The intrinsic movement of the Class II YSOs on the plane of the sky was calculated by subtracting the mean proper motions. Then the tangential velocities in l and b directions (in units of km s⁻¹) are calculated as follows:

$$\begin{aligned} v_l &= \kappa \frac{1}{\varpi} * (\mu_l - \bar{\mu}_l), \\ v_b &= \kappa \frac{1}{\varpi} * (\mu_b - \bar{\mu}_b), \end{aligned} \tag{8}$$

where $\kappa = 4.74$ km yr s⁻¹, ϖ is the parallax in units of mas, and μ_l and μ_b are the proper motion along the l and b directions, respectively, in units of mas yr⁻¹.

Figure 14 (b) shows the projected distributions and tangential velocities of the Class II YSOs. The Class II YSOs are mainly located in the molecular gas surrounding the bubble, and their motions are relatively random on the plane of the sky. Figure 15 shows P-V diagrams of the selected YSOs. There is no clear evidence of expansion in the figure. In order to determine whether the YSOs are expanding, we regard the expansion velocity as the radial outward component of the intrinsic velocity from the center of the bubble. The median expansion velocity of the Class II YSOs is found to be 0.0 ± 0.1 km s⁻¹. Therefore, the YSOs associated with the gas may not exhibit expansion on the plane of the sky.

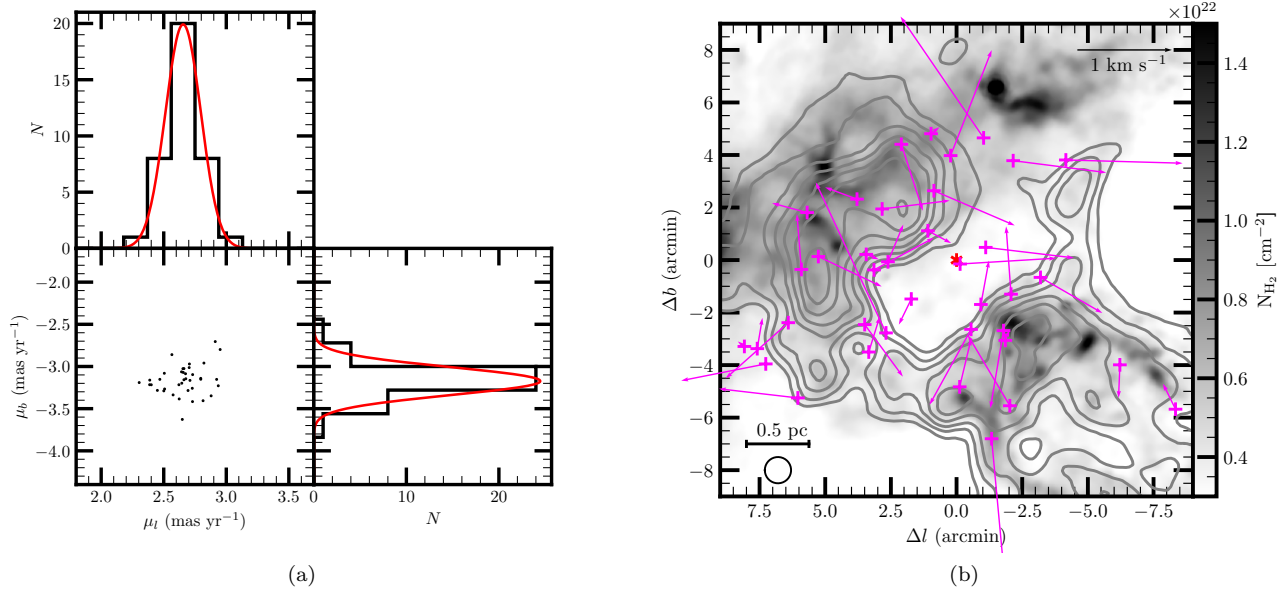


Figure 14. (a) Distribution of the proper motions of the YSOs, where the average proper motion of these sources is $(2.65, -3.17)$ mas yr^{-1} , and the 1σ uncertainty range of the Gaussian fitting is $(0.14, 0.17)$ mas yr^{-1} . (b) Projected distribution and tangential velocity of the YSOs. The magenta arrows depict the velocity for each YSO with respect to the mean velocity of the YSO sample. The red asterisk $(0, 0)$ is the center of the bubble.

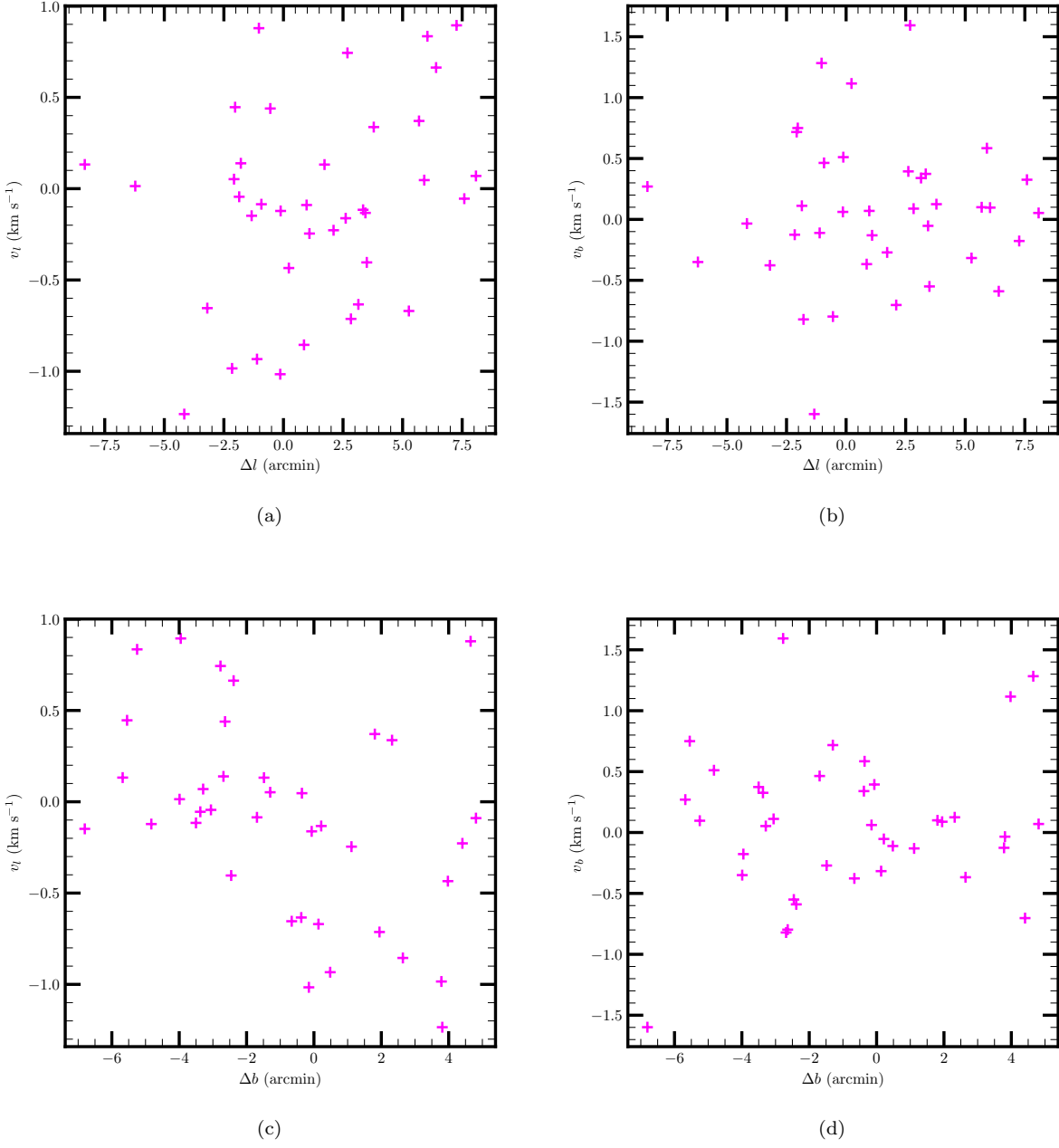


Figure 15. P-V diagrams of the Class II YSOs used to investigate the kinematic features.

5. SUMMARY

We observed four molecular lines (^{12}CO , ^{13}CO , C^{18}O , and $\text{HCO}^+ J = 1-0$), and collected YSOs in S Mon to investigate the bubble, an outflow identified in one of the clumps, as well as the energy cascade in the S Mon region. This includes the dynamical timescale, possible driving sources, and feedback of the outflow and bubble. The main results are summarized as follows.

- 1 The Class II YSOs are closely associated with the molecular gas in terms of spatial distribution and kinematic properties. According to the *Gaia* DR3 parallaxes of the Class II YSOs, we estimate the distance to S Mon to be $\sim 722 \pm 9$ pc.
- 2 We discover a molecular bubble in the S Mon region which is consistent with the *Herschel* H_2 column density maps. The molecular bubble has a radius of $\sim 1.1 \pm 0.1$ pc, a mass of $\sim 1\,400 \pm 400 M_\odot$, a momentum of $\sim 4\,600 \pm 1\,300 M_\odot \text{ km s}^{-1}$, and kinetic energy of $\sim (1.5 \pm 0.4) \times 10^{47}$ erg. The dynamical timescale of the H_{II} region of 15 Mon is $(3.5\text{--}8.9) \times 10^5$ yr, which is likely to be the main driving source of the bubble.
- 3 We detect a molecular outflow in the shell of the bubble, which indicates that star formation activity is ongoing around the bubble. The outflow has a mass of a few M_\odot , a momentum of a few tens of $M_\odot \text{ km s}^{-1}$, kinetic energy of $\sim 10^{45}$ erg, a dynamical timescale of $\sim 10^5$ yr, and a mechanical luminosity of a few times $10^{-1} L_\odot$.
- 4 The wind energy helps to sustain the turbulence in the S Mon region and drive the bubble. The bubble can also provide sufficient energy input to sustain the cloud turbulence. The measured outflow in clump E is enough to maintain the turbulence of the clump E. Outflows (like the one detected in clump E) could generally contribute to the turbulence of a cloud, while in S Mon further outflows are not yet confirmed.
- 5 The Class II YSOs correlated to the molecular bubble do not show expansion on the plane of the sky.

1 We appreciate the anonymous referee for the instructive comments that helped us to improve the paper. This work
 2 was funded by the NSFC Grants 11933011, National SKA Program of China (Grant No. 2022SKA0120103) and the
 3 Key Laboratory for Radio Astronomy. L.Y.J. thanks the support of the NSFC grant No. 12203104, the Natural
 4 Science Foundation of Jiangsu Province (grant No. BK20210999), the Entrepreneurship and Innovation Program of
 5 Jiangsu Province. This work has made use of data from the European Space Agency (ESA) mission *Gaia* (<https://www.cosmos.esa.int/gaia>)
 6 processed by the *Gaia* Data Processing and Analysis Consortium (DPAC, <https://www.cosmos.esa.int/web/gaia/dpac/consortium>). Funding for the DPAC has been provided by national institutions, in
 7 particular the institutions participating in the *Gaia* Multilateral Agreement.
 8

REFERENCES

- Abdurro'uf, Accetta, K., Aerts, C., et al. 2022, *ApJS*, 259, 35, doi: [10.3847/1538-4365/ac4414](https://doi.org/10.3847/1538-4365/ac4414)
- Arce, H. G., Borkin, M. A., Goodman, A. A., Pineda, J. E., & Beaumont, C. N. 2011, *ApJ*, 742, 105, doi: [10.1088/0004-637X/742/2/105](https://doi.org/10.1088/0004-637X/742/2/105)
- Arce, H. G., Borkin, M. A., Goodman, A. A., Pineda, J. E., & Halle, M. W. 2010, *ApJ*, 715, 1170, doi: [10.1088/0004-637X/715/2/1170](https://doi.org/10.1088/0004-637X/715/2/1170)
- Bally, J. 2016, *ARA&A*, 54, 491, doi: [10.1146/annurev-astro-081915-023341](https://doi.org/10.1146/annurev-astro-081915-023341)
- Bontemps, S., Andre, P., Terebey, S., & Cabrit, S. 1996, *A&A*, 311, 858
- Broos, P. S., Getman, K. V., Povich, M. S., et al. 2013, *ApJS*, 209, 32, doi: [10.1088/0067-0049/209/2/32](https://doi.org/10.1088/0067-0049/209/2/32)
- Buckle, J. V., Richer, J. S., & Davis, C. J. 2012, *MNRAS*, 423, 1127, doi: [10.1111/j.1365-2966.2012.20941.x](https://doi.org/10.1111/j.1365-2966.2012.20941.x)
- Castor, J., McCray, R., & Weaver, R. 1975, *ApJL*, 200, L107, doi: [10.1086/181908](https://doi.org/10.1086/181908)
- Chen, Y., Zhou, P., & Chu, Y.-H. 2013, *ApJL*, 769, L16, doi: [10.1088/2041-8205/769/1/L16](https://doi.org/10.1088/2041-8205/769/1/L16)
- Churchwell, E., Povich, M. S., Allen, D., et al. 2006, *ApJ*, 649, 759, doi: [10.1086/507015](https://doi.org/10.1086/507015)
- Cody, A. M., Stauffer, J., Baglin, A., et al. 2014, *AJ*, 147, 82, doi: [10.1088/0004-6256/147/4/82](https://doi.org/10.1088/0004-6256/147/4/82)
- Dahm, S. E. 2008, in *Handbook of Star Forming Regions*, Volume I, ed. B. Reipurth, Vol. 4, 966
- Dale, J. E. 2015, *NewAR*, 68, 1, doi: [10.1016/j.newar.2015.06.001](https://doi.org/10.1016/j.newar.2015.06.001)
- Dyson, J. E., & Williams, D. A. 1980, *Physics of the interstellar medium*
- Fazio, G. G., Hora, J. L., Allen, L. E., et al. 2004, *ApJS*, 154, 10, doi: [10.1086/422843](https://doi.org/10.1086/422843)
- Feddersen, J. R., Arce, H. G., Kong, S., et al. 2018, *ApJ*, 862, 121, doi: [10.3847/1538-4357/aacaf2](https://doi.org/10.3847/1538-4357/aacaf2)
- Feigelson, E. D., Townsley, L. K., Broos, P. S., et al. 2013, *ApJS*, 209, 26, doi: [10.1088/0067-0049/209/2/26](https://doi.org/10.1088/0067-0049/209/2/26)
- Fűrész, G., Hartmann, L. W., Megeath, S. T., Szentgyorgyi, A. H., & Hamden, E. T. 2008, *ApJ*, 676, 1109, doi: [10.1086/525844](https://doi.org/10.1086/525844)
- Flaccomio, E., Micela, G., Peres, G., et al. 2023, *A&A*, 670, A37, doi: [10.1051/0004-6361/202244872](https://doi.org/10.1051/0004-6361/202244872)
- Frank, A., Ray, T. P., Cabrit, S., et al. 2014, in *Protostars and Planets VI*, ed. H. Beuther, R. S. Klessen, C. P. Dullemond, & T. Henning, 451, doi: [10.2458/azu_uapress.9780816531240-ch020](https://doi.org/10.2458/azu_uapress.9780816531240-ch020)
- Gaia Collaboration, Prusti, T., de Bruijne, J. H. J., et al. 2016, *A&A*, 595, A1, doi: [10.1051/0004-6361/201629272](https://doi.org/10.1051/0004-6361/201629272)
- Gaia Collaboration, Vallenari, A., Brown, A. G. A., et al. 2023, *A&A*, 674, A1, doi: [10.1051/0004-6361/202243940](https://doi.org/10.1051/0004-6361/202243940)
- Garden, R. P., Hayashi, M., Gatley, I., Hasegawa, T., & Kaifu, N. 1991, *ApJ*, 374, 540, doi: [10.1086/170143](https://doi.org/10.1086/170143)
- Geen, S., Rosdahl, J., Blaizot, J., Devriendt, J., & Slyz, A. 2015, *MNRAS*, 448, 3248, doi: [10.1093/mnras/stv251](https://doi.org/10.1093/mnras/stv251)
- Gilmore, G., Randich, S., Asplund, M., et al. 2012, *The Messenger*, 147, 25
- Grady, C. A., Snow, T. P., & Cash, W. C. 1984, *ApJ*, 283, 218, doi: [10.1086/162296](https://doi.org/10.1086/162296)
- Green, G. M., Schlafly, E., Zucker, C., Speagle, J. S., & Finkbeiner, D. 2019, *ApJ*, 887, 93, doi: [10.3847/1538-4357/ab5362](https://doi.org/10.3847/1538-4357/ab5362)
- Greene, T. P., Wilking, B. A., Andre, P., Young, E. T., & Lada, C. J. 1994, *ApJ*, 434, 614, doi: [10.1086/174763](https://doi.org/10.1086/174763)
- Großschedl, J. E., Alves, J., Meingast, S., & Herbst-Kiss, G. 2021, *A&A*, 647, A91, doi: [10.1051/0004-6361/202038913](https://doi.org/10.1051/0004-6361/202038913)
- Großschedl, J. E., Alves, J., Meingast, S., et al. 2018, *A&A*, 619, A106, doi: [10.1051/0004-6361/201833901](https://doi.org/10.1051/0004-6361/201833901)
- Guo, H. L., Chen, B. Q., Yuan, H. B., et al. 2021, *ApJ*, 906, 47, doi: [10.3847/1538-4357/abc68a](https://doi.org/10.3847/1538-4357/abc68a)
- Hacar, A., Alves, J., Forbrich, J., et al. 2016, *A&A*, 589, A80, doi: [10.1051/0004-6361/201527805](https://doi.org/10.1051/0004-6361/201527805)
- Kerr, F. J., & Lynden-Bell, D. 1986, *MNRAS*, 221, 1023, doi: [10.1093/mnras/221.4.1023](https://doi.org/10.1093/mnras/221.4.1023)
- Lada, C. J. 1985, *ARA&A*, 23, 267, doi: [10.1146/annurev.aa.23.090185.001411](https://doi.org/10.1146/annurev.aa.23.090185.001411)
- Lada, C. J. 1987, in *Star Forming Regions*, ed. M. Peimbert & J. Jugaku, Vol. 115, 1
- Lada, C. J., & Wilking, B. A. 1984, *ApJ*, 287, 610, doi: [10.1086/162719](https://doi.org/10.1086/162719)
- Lada, C. J., Muench, A. A., Luhman, K. L., et al. 2006, *AJ*, 131, 1574, doi: [10.1086/499808](https://doi.org/10.1086/499808)
- Lallement, R., Babusiaux, C., Vergely, J. L., et al. 2019, *A&A*, 625, A135, doi: [10.1051/0004-6361/201834695](https://doi.org/10.1051/0004-6361/201834695)
- Lamers, H. J. G. L. M., & Cassinelli, J. P. 1999, *Introduction to Stellar Winds*
- Li, H., Li, D., Qian, L., et al. 2015, *ApJS*, 219, 20, doi: [10.1088/0067-0049/219/2/20](https://doi.org/10.1088/0067-0049/219/2/20)
- Li, Y., Li, F.-C., Xu, Y., et al. 2018, *ApJS*, 235, 15, doi: [10.3847/1538-4365/aaab67](https://doi.org/10.3847/1538-4365/aaab67)
- Li, Y., Xu, Y., Sun, Y., & Yang, J. 2020, *ApJS*, 251, 26, doi: [10.3847/1538-4365/abc34b](https://doi.org/10.3847/1538-4365/abc34b)
- Lindgren, L., Bastian, U., Biermann, M., et al. 2021, *A&A*, 649, A4, doi: [10.1051/0004-6361/202039653](https://doi.org/10.1051/0004-6361/202039653)
- Liu, D.-J., Xu, Y., Li, Y.-J., et al. 2021, *ApJS*, 253, 15, doi: [10.3847/1538-4365/abcece](https://doi.org/10.3847/1538-4365/abcece)
- Martins, F., Schaerer, D., & Hillier, D. J. 2005, *A&A*, 436, 1049, doi: [10.1051/0004-6361:20042386](https://doi.org/10.1051/0004-6361:20042386)
- McKee, C. F. 1989, *ApJ*, 345, 782, doi: [10.1086/167950](https://doi.org/10.1086/167950)

- McKee, C. F., & Ostriker, E. C. 2007, *ARA&A*, 45, 565, doi: [10.1146/annurev.astro.45.051806.110602](https://doi.org/10.1146/annurev.astro.45.051806.110602)
- Montillaud, J., Juvela, M., Vastel, C., et al. 2019, *A&A*, 631, A3, doi: [10.1051/0004-6361/201834903](https://doi.org/10.1051/0004-6361/201834903)
- Nakamura, F., & Li, Z.-Y. 2007, *The Astrophysical Journal*, 662, 395, doi: [10.1086/517515](https://doi.org/10.1086/517515)
- Nakamura, F., & Li, Z.-Y. 2014, *ApJ*, 783, 115, doi: [10.1088/0004-637X/783/2/115](https://doi.org/10.1088/0004-637X/783/2/115)
- Nony, T., Robitaille, J. F., Motte, F., et al. 2021, *A&A*, 645, A94, doi: [10.1051/0004-6361/202039353](https://doi.org/10.1051/0004-6361/202039353)
- Perryman, M. A. C., Lindegren, L., Kovalevsky, J., et al. 1997, *A&A*, 323, L49
- Pety, J. 2005, in *SF2A-2005: Semaine de l'Astrophysique Francaise*, ed. F. Casoli, T. Contini, J. M. Hameury, & L. Pagani, 721
- Pilbratt, G. L., Riedinger, J. R., Passvogel, T., et al. 2010, *A&A*, 518, L1, doi: [10.1051/0004-6361/201014759](https://doi.org/10.1051/0004-6361/201014759)
- Randich, S., Gilmore, G., & Gaia-ESO Consortium. 2013, *The Messenger*, 154, 47
- Rapson, V. A., Pipher, J. L., Gutermuth, R. A., et al. 2014, *ApJ*, 794, 124, doi: [10.1088/0004-637X/794/2/124](https://doi.org/10.1088/0004-637X/794/2/124)
- Reid, M. J., Menten, K. M., Zheng, X. W., et al. 2009, *ApJ*, 700, 137, doi: [10.1088/0004-637X/700/1/137](https://doi.org/10.1088/0004-637X/700/1/137)
- Rieke, G. H., Young, E. T., Engelbracht, C. W., et al. 2004, *ApJS*, 154, 25, doi: [10.1086/422717](https://doi.org/10.1086/422717)
- Shan, W., Yang, J., Shi, S., et al. 2012, *IEEE Transactions on Terahertz Science and Technology*, 2, 593, doi: [10.1109/TTHZ.2012.2213818](https://doi.org/10.1109/TTHZ.2012.2213818)
- Simon, R., Jackson, J. M., Clemens, D. P., Bania, T. M., & Heyer, M. H. 2001, *ApJ*, 551, 747, doi: [10.1086/320230](https://doi.org/10.1086/320230)
- Skrutskie, M. F., Cutri, R. M., Stiening, R., et al. 2006, *AJ*, 131, 1163, doi: [10.1086/498708](https://doi.org/10.1086/498708)
- Snow, T. P., J., Cash, W., & Grady, C. A. 1981, *ApJL*, 244, L19, doi: [10.1086/183470](https://doi.org/10.1086/183470)
- Sun, J. X., Lu, D. R., Yang, J., et al. 2018, *Acta Astronomica Sinica*, 59, 3
- Sung, H., & Bessell, M. S. 2010, *AJ*, 140, 2070, doi: [10.1088/0004-6256/140/6/2070](https://doi.org/10.1088/0004-6256/140/6/2070)
- Sung, H., Bessell, M. S., Chun, M.-Y., Karimov, R., & Ibrahimov, M. 2008, *AJ*, 135, 441, doi: [10.1088/0004-6256/135/2/441](https://doi.org/10.1088/0004-6256/135/2/441)
- Sung, H., Stauffer, J. R., & Bessell, M. S. 2009, *AJ*, 138, 1116, doi: [10.1088/0004-6256/138/4/1116](https://doi.org/10.1088/0004-6256/138/4/1116)
- Tauber, J. A., Lis, D. C., & Goldsmith, P. F. 1993, *ApJ*, 403, 202, doi: [10.1086/172194](https://doi.org/10.1086/172194)
- Teixeira, P. S., Lada, C. J., Marengo, M., & Lada, E. A. 2012, *A&A*, 540, A83, doi: [10.1051/0004-6361/201015326](https://doi.org/10.1051/0004-6361/201015326)
- Tobin, J. J., Hartmann, L., Fűrész, G., Hsu, W.-H., & Mateo, M. 2015, *AJ*, 149, 119, doi: [10.1088/0004-6256/149/4/119](https://doi.org/10.1088/0004-6256/149/4/119)
- Tobin, J. J., Hartmann, L., Furesz, G., Mateo, M., & Megeath, S. T. 2009, *ApJ*, 697, 1103, doi: [10.1088/0004-637X/697/2/1103](https://doi.org/10.1088/0004-637X/697/2/1103)
- Turner, B. E., Pirogov, L., & Minh, Y. C. 1997, *ApJ*, 483, 235, doi: [10.1086/304228](https://doi.org/10.1086/304228)
- Venuti, L., Prisinzano, L., Sacco, G. G., et al. 2018, *A&A*, 609, A10, doi: [10.1051/0004-6361/201731103](https://doi.org/10.1051/0004-6361/201731103)
- Walch, S. K., Whitworth, A. P., Bisbas, T., Wünsch, R., & Hubber, D. 2012, *MNRAS*, 427, 625, doi: [10.1111/j.1365-2966.2012.21767.x](https://doi.org/10.1111/j.1365-2966.2012.21767.x)
- Weisskopf, M. C., Brinkman, B., Canizares, C., et al. 2002, *PASP*, 114, 1, doi: [10.1086/338108](https://doi.org/10.1086/338108)
- Xu, J.-L., Xu, Y., Yu, N., et al. 2017, *ApJ*, 849, 140, doi: [10.3847/1538-4357/aa8ee0](https://doi.org/10.3847/1538-4357/aa8ee0)
- Yang, A. Y., Thompson, M. A., Urquhart, J. S., & Tian, W. W. 2018, *ApJS*, 235, 3, doi: [10.3847/1538-4365/aaa297](https://doi.org/10.3847/1538-4365/aaa297)
- Zhang, M. 2023, *ApJS*, 265, 115, doi: [10.1088/0004-637X/783/2/115](https://doi.org/10.1088/0004-637X/783/2/115)
- Zhang, Q., Wang, K., Lu, X., & Jiménez-Serra, I. 2015, *ApJ*, 804, 141, doi: [10.1088/0004-637X/804/2/141](https://doi.org/10.1088/0004-637X/804/2/141)
- Zucker, C., Speagle, J. S., Schlafly, E. F., et al. 2020, *A&A*, 633, A51, doi: [10.1051/0004-6361/201936145](https://doi.org/10.1051/0004-6361/201936145)

APPENDIX

A. YSO CLASSIFICATION SCHEME

We describe the classification scheme for YSOs in this section. The YSO candidates in S Mon are collected from the catalogs of [Sung et al. \(2009\)](#), [Broos et al. \(2013\)](#), [Cody et al. \(2014\)](#), and [Rapson et al. \(2014\)](#), within a field of $202.8^\circ < l < 203.1^\circ$, $2.0^\circ < b < 2.3^\circ$. We consider two stars separated by less than $1''$ to be the same star, and remove duplicated YSO candidates. A total of 1 023 YSO candidates were initially selected. However, this initial catalog not only included numerous samples that were not YSOs, but also the YSOs in the catalog were obtained through different classification schemes. To maintain the homogeneity of the YSO catalog, we classified the YSO candidates based on a homogeneous method.

We applied the spectral index of the SED to classify the evolutionary stage of the YSOs, where $\alpha = d \log \lambda F_\lambda / d \log \lambda$ ([Greene et al. 1994](#)). To build this scheme, we use photometric data from the 2MASS K_s band ([Skrutskie et al. 2006](#)), four IRAC bands (3.6, 4.2, 5.8, and $8.0 \mu\text{m}$) of *Spitzer* ([Fazio et al. 2004](#)), and the MIPS $24 \mu\text{m}$ band ([Rieke et al. 2004](#)). Note that not all six bands are required simultaneously for the classification; however, at least three IRAC bands are necessary. Only sources with photometric uncertainties $\sigma < 0.2$ mag were selected for classification. Finally, we compiled a sample of seven Class I, 160 Class II, and 245 Class III YSOs. Figure 16 shows color-color diagrams of the classified YSOs in the S Mon region.

To obtain the parallaxes and proper motions of the classified YSOs, we cross matched them with stars in *Gaia* DR3 within $1''$. One Class I, 145 Class II and 231 Class III YSOs were assigned astrometric parameters from *Gaia* DR3.

In the next step we added RV data to our YSO sample. First, we checked the availability of *Gaia* DR3 RVs. There were only 16 YSOs with measured *Gaia* DR3 RVs, of which most fell outside the velocity range of interest (about 63% are beyond the range of $0\text{--}15 \text{ km s}^{-1}$), and/or they had large RV uncertainties. Therefore, we did not use *Gaia* RVs in our analysis. The RVs of the classified YSOs were collected from APOGEE-2 DR17 ([Abdurro'uf et al. 2022](#)) and the catalog of [Tobin et al. \(2015\)](#), who measured the RVs of 695 stars in NGC 2264 (using multi-fiber echelle spectroscopy at the 6.5 m MMT and *Magellan* telescopes). We cross matched our YSO candidates (1 023) with the APOGEE catalog using the `source_id` in the *Gaia* DR3 catalog, and with the catalog of [Tobin et al. \(2015\)](#) within $1''$, yielding 73 YSOs with RVs from APOGEE and 148 YSOs with RVs from [Tobin et al. \(2015\)](#). A total of 44 YSO candidates were matched in both catalogs. We made a comparison of the V_{LSR} (converted from heliocentric RVs to RVs relative to the local standard of rest, LSR) collected from the two catalogs for the YSO candidates, as shown in Figure 17. The average difference between them is 0.7 km s^{-1} , and the 1σ dispersion is 1.0 km s^{-1} . The Pearson's correlation coefficient between them is 0.99. We therefore added the RVs from [Tobin et al. \(2015\)](#) to our sample and applied a systematic shift of 0.7 km s^{-1} , applied because the RV errors in the APOGEE catalog are consistently smaller than those in the catalog of [Tobin et al. \(2015\)](#). Finally, we obtained 47 Class II, and 91 Class III YSOs with RVs.

To sum up, we obtained seven Class I, 160 Class II, and 245 Class III YSOs in the S Mon region. Among them, one Class I, 145 Class II, and 231 Class III YSOs have counterparts in *Gaia* DR3, where 47 Class II and 91 Class III YSOs have RVs. Table 5 describes the YSO samples.

B. CALCULATION OF THE PHYSICAL PARAMETERS

In this study, the properties of the molecular gas are estimated under the assumption that all of the molecular gas is in LTE. Optically thin ^{13}CO lines are employed to estimate the column density and mass of the molecular gas. According to [Garden et al. \(1991\)](#), the ^{13}CO column density can be estimated via:

$$N(^{13}\text{CO}) = 4.71 \times 10^{13} \frac{T_{\text{ex}} + 0.88}{\exp(-5.29/T_{\text{ex}})} \times \frac{\tau}{1 - \exp(-\tau)} \int T_{\text{mb},13} dv, \quad (\text{B1})$$

where τ is the optical depth, T_{ex} is the mean excitation temperature of the molecular gas, and $T_{\text{mb},13}$ is the main-beam temperature of ^{13}CO .

We assume that the ^{12}CO emission is optically thick. The excitation temperature, T_{ex} , can be estimated by ([Garden et al. 1991](#)):

$$T_{\text{ex}} = \frac{5.53}{\ln [1 + 5.53 / (T_{\text{mb},12} + 0.82)]}, \quad (\text{B2})$$

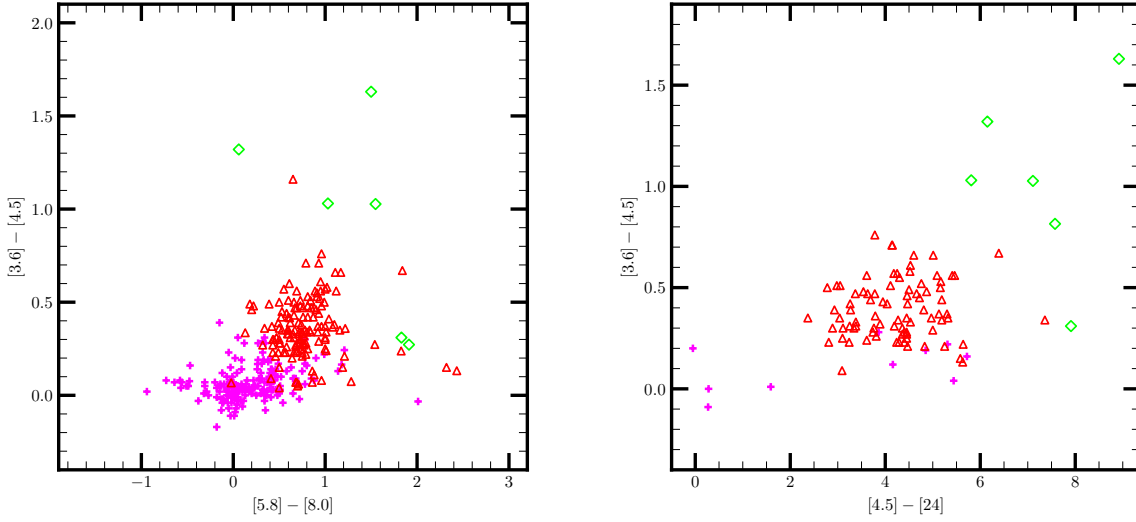


Figure 16. Color-color diagrams showing the classified YSOs. The green diamonds, red triangles, and magenta crosses present Class I, Class II, Class III YSOs, respectively.

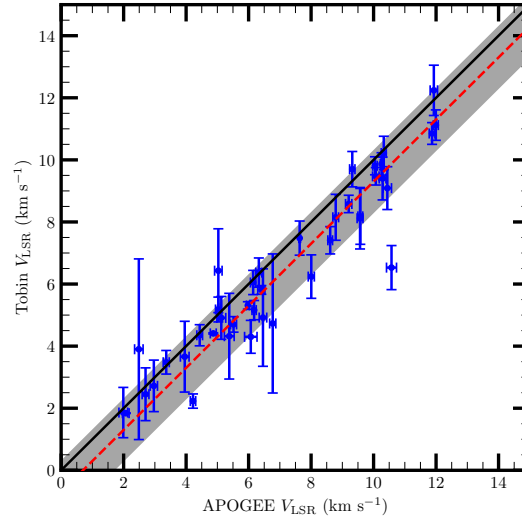


Figure 17. Comparison of the V_{LSR} values in the APOGEE and Tobin et al. (2015) samples. The black line represents where V_{LSR} is the same in both catalogs. The red dashed line indicates the mean value of the difference between the APOGEE and Tobin et al. (2015) V_{LSR} values, and the gray filled region depicts the corresponding 1σ region.

where $T_{\text{mb},12}$ is the peak main-beam temperature of ^{12}CO .

The optical depth can be derived using the following equation (Garden et al. 1991):

$$\tau(^{13}\text{CO}) = -\ln \left[1 - \frac{T_{\text{mb},13}}{5.29/[\exp(5.29/T_{\text{ex}}) - 1] - 0.89} \right]. \quad (\text{B3})$$

The relation $N_{\text{H}_2}/N_{^{13}\text{CO}} \approx 5 \times 10^5$ (Simon et al. 2001) is used to estimate the H_2 column density. The mass, M , can be determined by:

$$M = \mu m_{\text{H}} N(\text{H}_2) S, \quad (\text{B4})$$

Table 5. Description of the YSO Samples

Column	Format	Unit	Description
ID	A4	—	ID
Gaia	I19	—	Gaia DR3 identifier
RAdeg	F8.4	deg	Right ascension (J2000)
DEdeg	F8.4	deg	Declination (J2000)
plx	F7.3	mas	Gaia DR3 parallax
e_plx	F7.3	mas	Uncertainty in the parallax
pmRA	F7.3	mas/yr	Proper motion in the RA* direction
e_pmRA	F7.3	mas/yr	Uncertainty in pmRA
pmDE	F7.3	mas/yr	Proper motion in the DEC direction
e_pmDE	F7.3	mas/yr	Uncertainty in pmDE
Vlsr	F7.1	km/s	LSR velocity
e_Vlsr	F7.1	km/s	Uncertainty in the LSR velocity
Jmag	F5.2	mag	2MASS J band magnitude
e_Jmag	F5.2	mag	Uncertainty in Jmag
Hmag	F5.2	mag	2MASS H band magnitude
e_Hmag	F5.2	mag	Uncertainty in Hmag
Ksmag	F5.2	mag	2MASS Ks band magnitude
e_Ksmag	F5.2	mag	Uncertainty in Ksmag
3.6mag	F5.2	mag	Spitzer/IRAC 3.6 micron band magnitude
e_3.6mag	F5.2	mag	Uncertainty in 3.6mag
4.5mag	F5.2	mag	Spitzer/IRAC 4.5 micron band magnitude
e_4.5mag	F5.2	mag	Uncertainty in 4.5mag
5.8mag	F5.2	mag	Spitzer/IRAC 5.8 micron band magnitude
e_5.8mag	F5.2	mag	Uncertainty in 5.8mag
8.0mag	F5.2	mag	Spitzer/IRAC 8.0 micron band magnitude
e_8.0mag	F5.2	mag	Uncertainty in 8.0mag
24mag	F5.2	mag	Spitzer/MIPS 24 micron band magnitude
e_24mag	F5.2	mag	Uncertainty in 24mag
Class	A10	—	Source classification
OClass	A10	—	Other source classification
Ref	A15	—	Reference
Ref_RV	A15	—	Reference for the LSR velocity

NOTE—This table is available in its entirety in machine-readable form.

where $\mu = 2.72$ is the mean molecular weight, m_{H} is the mass of the hydrogen atom (Garden et al. 1991), and S is the projected 2D area.

The turbulent energy, E_{turb} , can be given approximately by:

$$E_{\text{turb}} = \frac{1}{2} M \sigma_{3\text{d}}^2, \quad (\text{B5})$$

where σ_{3d} is the 3D turbulent velocity dispersion, which can be calculated by:

$$\sigma_{3d} = \sqrt{3}\sigma_{1d} = \frac{\sqrt{3}}{2\sqrt{2\ln 2}}\Delta V_{\text{FWHM}}, \quad (\text{B6})$$

where ΔV_{FWHM} is the 1D FWHM velocity dispersion based on typical ^{13}CO .

The gravitational binding energy, E_{grav} , can be calculated by:

$$E_{\text{grav}} = \frac{GM^2}{R}, \quad (\text{B7})$$

where R is the radius.

The excitation temperatures of the eight clumps are between 21.3 and 33.2 K. Since these clumps are regularly located within the bubble, a mean excitation temperature of about 26.9 K is adopted as that of the bubble. The mean column density of the bubble is $\sim 2.5 \times 10^{20} \text{ cm}^{-2}$ and its mass is $\sim 1400 M_{\odot}$. In this work, we consider the uncertainties in gas temperature, shell region, and distance for the shell mass estimation. The total uncertainty caused by these factors is about $\pm 400 M_{\odot}$.

Figure 18 shows the projected area of the cloud. The red lines denoted its boundary, determined by pixels whose main-beam brightness temperature is larger than $3 \times \text{rms}$ in at least three successive channels. The velocity range adopted here is between 7 and 15 km s^{-1} and the mass of the cloud is derived as $2200 \pm 500 M_{\odot}$. The uncertainties in the excitation temperature and distance are considered in the estimation of the cloud mass. σ_{1d} is obtained from Gaussian fitting of the average ^{13}CO line, which is about $1.0 \pm 0.1 \text{ km s}^{-1}$. The turbulent energy and gravitational binding energy of the cloud are estimated by Equation (B5) and Equation (B7), respectively, which correspond to $(6.3 \pm 2.5) \times 10^{46} \text{ erg}$ and $(2.1 \pm 1.0) \times 10^{47} \text{ erg}$.

The clump's column density (N_{H_2}), mass (M_{clump}), turbulent energy ($E_{\text{turb,clump}}$), and gravitational binding energy ($E_{\text{grav,clump}}$) were calculated using the same equations as applied to the cloud. The uncertainties in the distance and clump region were considered in the calculation.

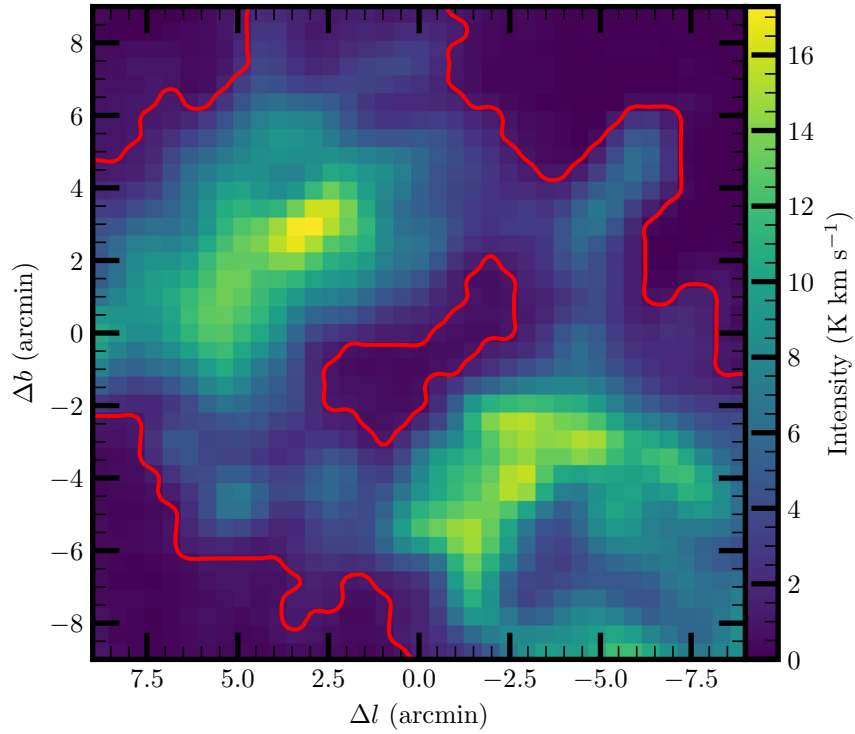


Figure 18. Intensity map of ^{13}CO for the velocity range 7–15 km s^{-1} . The red lines depict the boundary of the cloud.

C. DISTRIBUTION OF OB STARS

Figure 19 shows the projected distributions and relative proper motions of the O- and B-type stars in the S Mon region. Table 6 lists the parameters of these stars, which are collected from SIMBAD. The astrometry parameters of 15 Mon are from *Hipparcos* catalog (Perryman et al. 1997), and those of other sources are from *Gaia* DR3 (Gaia Collaboration et al. 2023).

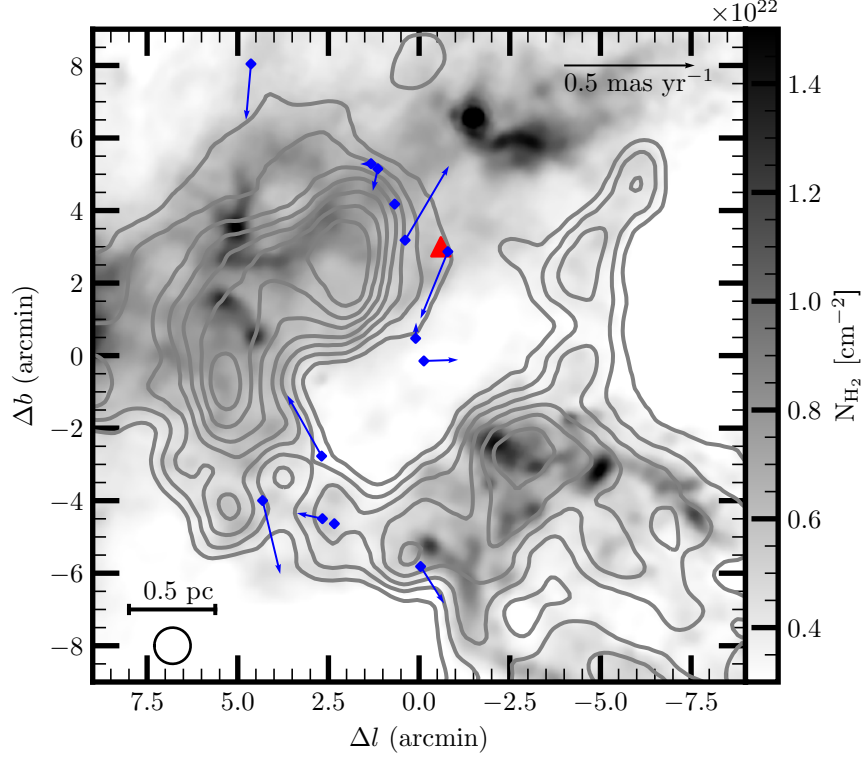


Figure 19. Projected distributions and relative proper motions of the O-(red triangle) and B-type (blue diamonds) stars. The average proper motion utilized being $(2.65, -3.17)$ mas yr $^{-1}$.

Table 6. Summary of the Parameters of the O- and B-type Stars

Identifier	SpType	α (deg)	δ (deg)	ϖ (mas)	σ_{ϖ} (mas)	$\mu_{\alpha} \cos \delta$ (mas yr $^{-1}$)	$\sigma_{\mu_{\alpha} \cos \delta}$ (mas yr $^{-1}$)	μ_{δ} (mas yr $^{-1}$)	$\sigma_{\mu_{\delta}}$ (mas yr $^{-1}$)	Gaia DR3 ID
(1)	(2)	(3)	(4)	(5)	(6)	(7)	(8)	(9)	(10)	(11)
15 Mon [†]	O7V+B1.5/2V	100.2444	9.8958	3.550	0.500	-2.610	0.560	-1.610	0.390	3326740865570982400
15 Mon B	B1.5/2V	100.2440	9.8951	1.402	0.098	-1.971	0.113	-4.225	0.082	3326740865571935232
V* V641 Mon	B1.5IV+(B2V)	100.1191	9.8179	1.389	0.045	-1.943	0.051	-3.775	0.040	3326716813754146176
LS VI +09 13	B1V	100.1552	9.7916	3326716470156761472
V* V684 Mon	B2.5V	100.1599	9.7878	1.540	0.041	-1.482	-0.050	-3.960	-0.041	3326715714242517248
HD 47961	B2.5V	100.3638	9.8540	1.248	0.079	-1.976	0.091	-4.034	0.077	3326737120359493504
HD 261810	B2.5Vn	100.1801	9.7671	1.424	0.033	-2.172	0.042	-3.942	0.033	3326715439364610816
HD 261938	B3V	100.2578	9.8800	1.540	0.059	-1.258	0.056	-3.247	0.041	3326740693772848896
EM* LkHA 25	B4Ve	100.1860	9.8006	1.414	0.111	-1.076	0.140	-3.826	0.125	3326715851681467904
HD 261878	B6V	100.2148	9.8637	1.331	0.037	-1.504	0.041	-3.747	0.030	3326717260430731648
CSI+09-06383	B7	100.2750	9.8833
HD 261841	B8IV-Ve	100.2037	9.8623	1.408	0.021	-1.722	0.023	-3.568	0.018	3326717226070995328
HD 261969	B9IV	100.2933	9.8838	1.351	0.036	-1.744	0.032	-3.916	0.028	3326740006577519360
NGC 2264 181	B9Vn	100.2968	9.8821	1.346	0.029	-1.576	-0.032	-3.880	0.027	3326740002281694592

NOTE—(1) Identifier. (2) Spectral type. (3) Right ascension (J2000). (4) Declination (J2000). (5) Parallax. (6) Uncertainty in parallax; (7) Proper motion in RA* direction. (8) Uncertainty in $\mu_{\alpha} \cos \delta$. (9) Proper motion in DEC direction. (10) Uncertainty in μ_{δ} . (11) Gaia DR3 identifier.

[†]: The astrometry parameters of 15 Mon (HIP 31978) are from *Hipparcos* catalog, and those of other sources are from Gaia DR3.